Organic Single-Crystalline Semiconductors for Light-Emitting Applications: Recent Advances and Developments

Ran Ding, Ming-Hui An, Jing Feng, and Hong-Bo Sun**

Organic single-crystalline semiconductors (OSCSs), as a vital branch of organic semiconductors, have recently attracted intense interest due to their numerous advantages such as highly ordered structure, high carrier mobility, high thermal stability, and low impurity levels, and they have worldwide use in different kinds of applications. In particular, the nature of better luminescence properties and remarkable charge-transport characteristics is a prerequisite for light-emitting aspects. Here, a concise overview of the recent progress on OSCSs research is provided, highlighting the prominent properties of OSCSs which are pertinent to light-emitting behavior. Various crystal-growth strategies are surveyed for the preparation of high-quality OSCSs via solution, melting, and vapor phases. Two typical electrical-pumping light-emitting devices, including organic light-emitting transistors and organic light-emitting diodes, are summarized with recent advances and developments exhibiting the latent potentialities of OSCSs in optoelectronics.

1. Introduction

The history of organic semiconductors dates back to the 1940s, which represent a large class of organic solids containing small-molecule compounds and polymers.[1–3] These materials have attracted much applied and fundamental research, and they have several promising advantages.[4–13] The facile low-temperature processing, together with their mechanical flexibility, approaches for flexible and foldable organic electronics.[14,15] Also, their solution-processing capability enables the realization of low-cost and large-area devices.[16–19] In particular, the easy strategies for material synthesis allow appropriate structural modifications to tune their solubility, polarity, band structure, charge carrier mobility, and so on.[20,21] Unlike their inorganic counterparts with continuous energy bands, organic semiconductors possess discrete energy levels where the occupied and unoccupied molecular orbitals are not closely packed. The charge transfer in organic semiconductors strongly relies on the conductivity, which is most relevant to the π-bonding orbitals and quantum mechanical wavefunction overlapping, namely, the energy levels of the highest occupied molecular orbital (HOMO) and the lowest unoccupied molecular orbital (LUMO), and the energy bandgap between them. To date, a vast number of organic molecular and polymeric semiconductors has been designed and synthesized for their technological relevance and potential advantages as mentioned for next-generation organic electronics.[22–24]

Among them, organic single-crystalline semiconductors (OSCSs) constructed by π-conjugated molecules in long-range periodic order have emerged as a unique optoelectrical material.[25–35] Their defined structures provide an opportunity to investigate the impact of the basic molecular interactions on the structure–property relationships and reveal fundamental physics in organic semiconductors. Also, the additional features of OSCSs, such as low impurity levels, high carrier mobility, and high thermal stability, make them more attractive in the field of optoelectronics. In early research, OSCSs served as a powerful tool for evaluating the intrinsic charge-transport mechanisms of organic semiconductors. The surface charge transport of these materials was determined based on the technology of field-effect transistors with recorded mobility reaching up to 43 $cm^2\ V^{-1}\ s^{-1}$.[25,36] Later, they have emerged as a hotspot in the field of optically pumped lasers, which stemmed from the discovery of amplified spontaneous emission (ASE) phenomena and lasing oscillations.[28,29,32] Also, electroluminescent (EL) devices based on organic semiconductors date back to 1963 when the first used materials were also OSCSs.[37] When searching Web of Science with the term "organic single crystals," more than 41 000 publications can be found within the last half century. This enthusiasm for the study of OSCSs has extended the applications range to various high-performance and low-cost

Dr. R. Ding, M.-H. An, Prof. J. Feng, Prof. H.-B. Sun
State Key Laboratory on Integrated Optoelectronics
College of Electronic Science and Engineering
Jilin University
2699 Qianjin Street, Changchun 130012, China
E-mail: jingfeng@jlu.edu.cn; hbsun@jlu.edu.cn; hbsun@tsinghua.edu.cn

Dr. R. Ding
Department of Applied Physics
The Hong Kong Polytechnic University
Hung Hom, Hong Kong, China

Prof. H.-B. Sun
State Key Lab of Precision Measurement Technology and Instruments,
Department of Precision Instrument
Tsinghua University
Haidian, Beijing 100084, China

The ORCID identification number(s) for the author(s) of this article can be found under https://doi.org/10.1002/lpor.201900009

DOI: 10.1002/lpor.201900009

optoelectronic devices. A series of broad reviews highlighting the most important progress obtained by OSCSs has finished in different aspects including growth strategies, materials design, and device applications.[25–35] However, none of the reviews so far has focused on the electrical-pumping light-emitting behavior, which is not only scientifically important but also technologically imperative for EL devices.

Here, we briefly outline the recent theoretical and experimental studies of the optoelectronic properties of OSCSs, especially from the perspective of stacking modes, charge transport, luminescence, and anisotropy, which are the key points for their light-emitting behaviors. A deeper understanding of these properties is a benefit for the development of rational molecular design and engineering strategies for performance optimization of OSCSs. We then review the various crystal-growth strategies to prepare high-quality OSCSs via solution, melting, and vapor phases, which contributes much to the rapid development of OSCS-based light-emitting devices. In addition, the recent progress with regard to electrical-pumping light-emitting applications are summarized including two typical OSCS-based devices, that is, organic light-emitting diodes (OLEDs) and organic light-emitting transistors (OLETs). Finally, a brief outlook on the current challenges and future development opportunities of OSCSs for optoelectronic applications is presented.

2. Optoelectronic Properties of OSCSs

2.1. Molecular Stacking Properties

In OSCSs, identical molecules stack regularly and compactly by specific intermolecular interactions, which play a key role regarding the optical and electrical properties. As a prerequisite for high-performance organic light-emitting devices, the materials must possess both better luminescence properties and optimal charge-transport characteristics. A rigorous description of the principles of molecular packing mode is beneficial for understanding the structure–property relationship and development of rational molecular design.

The excitonic interactions of neighboring molecules in the aggregate state will strongly influence the material photophysical properties.[38] These exciton effects can be revealed using the theory of molecular-exciton coupling originally developed by Kasha and co-workers for understanding absorption and fluorescence in aggregates of conjugated oligomers.[39–41] It is proposed that these excitonic interactions are determined by Coulombic coupling of the transition dipole densities which are strongly associated with the spatial distribution of the constituent molecules.[42–46] The classification of H- versus J-aggregation has been proved to be a key development in elucidating the relationship between morphology and photophysics. As depicted in **Figure 1**a,b, molecular side-by-side orientations belong to H-aggregation with a positive resonant excitonic coupling, whereas head-to-tail orientations are J-aggregation and the couplings are negative. The energy dispersion, $E(k)$, corresponding to the lowest vibronic band and the band curvature at $k = 0$, which is positive for J-aggregates and negative for H-aggregates, are also shown. In H-aggregates, the lowest-energy exciton lies at $k = \pi$, where the exciton ($k = 0$) is optically forbidden, thereby preventing 0–0 emission. Phonons with wavevector q derive from the intramolecular vibrations with energy $\hbar\omega_0$. Arrows indicate the emission pathways at low temperatures. As a result, blueshifted absorption spectra and luminescence quenching will arise from the rapid intraband relaxation in comparison to the isolated monomer. Conversely, in J-aggregates, the Frenkel exciton

Ran Ding received his B.S. and Ph.D. degrees from the School of Electronic Science and Engineering at Jilin University in 2010 and 2015, respectively. In 2016, he worked as a research fellow at Nanyang Technological University, Singapore. In 2018, he had a postdoctoral position at the Department of Applied Physics, The Hong Kong Polytechnic University. His research interests include organic single crystals, hybrid organic–inorganic metal perovskite materials and their functional devices.

Jing Feng received her B.S. and Ph.D. degrees in microelectronics and solid-state electronics from Jilin University in 1997 and 2003, respectively. She worked as a postdoctoral researcher at RIKEN, Japan, from 2003 to 2006. She joined Jilin University in 2006, where she is a professor at the College of Electronic Science and Engineering and State Key Laboratory on Integrated Optoelectronics. Her research focuses on organic optoelectronic devices.

Hong-Bo Sun received his B.S. and Ph.D. degrees in electronics from Jilin University, China, in 1992 and 1996, respectively. He worked as a postdoctoral researcher at Satellite Venture Business Laboratory, at the University of Tokushima, Japan, from 1996 to 2000, and then as an assistant professor in the Department of Applied Physics at Osaka University, Osaka, Japan. In 2005, he was promoted as a full professor (Changjiang Scholar) at Jilin University, China. In 2017, he joined Tsinghua University as a professor. His research interests are focused on ultrafast optoelectronics, particularly on laser nanofabrication and ultrafast spectroscopy.

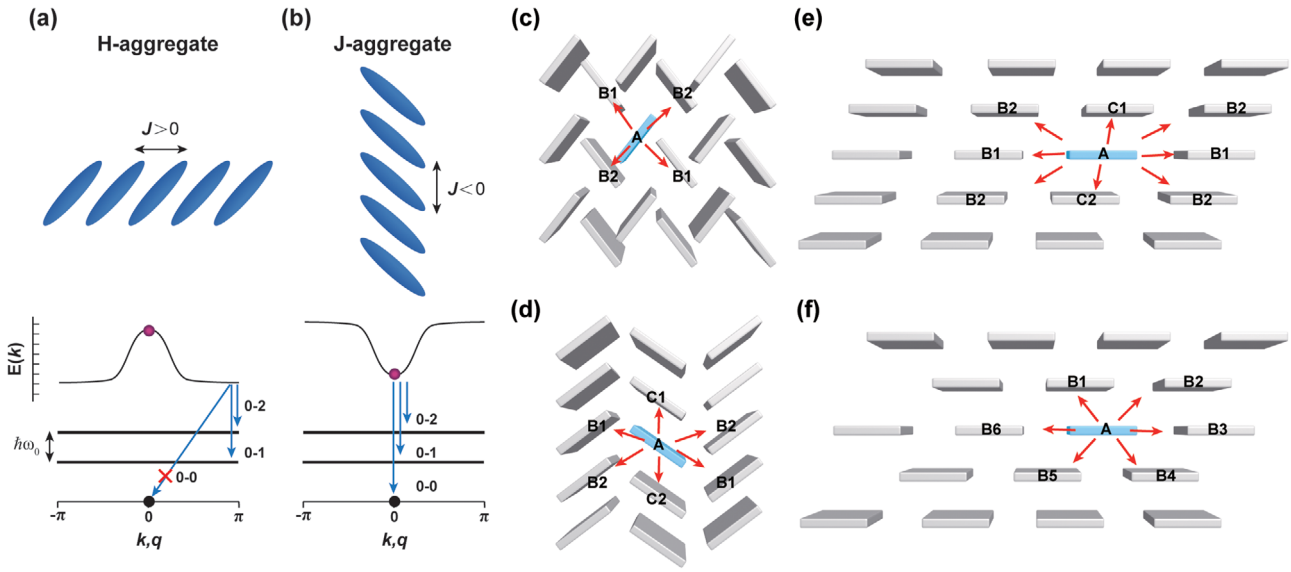

Figure 1. a,b) Molecular orientations within conventional H-aggregates (a) and J-aggregates (b). The sign of the nearest-neighbor coupling J is determined by the through-space Coulombic coupling. Generally, side-by-side orientations lead to $J > 0$ and H-aggregation, whereas head-to-tail orientations lead to $J < 0$ and J-aggregation. The band curvature at $k = 0$ is positive in H-aggregates and negative in J-aggregates. The energy dispersion $E(k)$ corresponding to the lowest vibronic band in each aggregate is shown. The phonons with wavevector q are derived from the intramolecular vibrations with energy $\hbar\omega_0$. The arrows indicate the emission pathways at low temperatures. a,b) Adapted with permission.[46] Copyright 2016, American Chemical Society. c–f) Schematic images of four typical molecular packing modes of organic molecules in the solid state and the possible charge-transport pathways in each case. c–f) Adapted with permission.[34] Copyright 2013, Wiley-VCH.

($k = 0$) at the bottom of the exciton band is optically allowed from the ground state, giving rise to redshifted absorption spectra and enhanced luminescence quantum yields because of the strong 0–0 emission. In addition, the oscillator strength can be concentrated in the lowest excited state, which will increase the high emission efficiency and the possibility of spontaneous emission. Moreover, the excited-state radiative decay rate is found to be enhanced in J-aggregation and suppressed in H-aggregation. The impact of such excitonic interactions on the material photophysics is related to the molecular dipole packing, which relies on both the molecular stacking mode and the transition dipole orientation direction in molecules. However, the widely existing H-aggregates in conjugated oligomer materials have constituted a major hindrance for light-emitting applications because of their mutually parallel molecular stacking and the fixed molecular dipole direction along the molecular long axes. Therefore, an appropriate molecular stacking mode with weak molecular transition dipole interaction is a fundamental requirement for achieving organic semiconductors with high luminescence efficiency. Theoretically speaking, the most effective method to weaken the interdipole interaction is to increase the spatial displacement of adjacent molecules. Four different molecular stacking modes have been attempted, including the movements of one molecule along the chain-axis direction, in-plane transverse axis, rotation around the molecular long axis, and rotation around the stacking axis. Their energy-splitting degree of molecular orbits has also been evaluated.[47,48] Among them, the rotation of one molecule around the stacking axis is the most ideal way, and it is much easier for the excited-state transition and beneficial to promote the emission efficiency. It is supposed that the interdipole coupling can be neglected while the angle rotated up to 90°. Then, the aggregates will endow with the same emission properties as isolated molecules in solution.

It is noted that optimizing the charge-transfer integrals is an effective strategy for improving charge-carrier transport due to the enhanced electronic couplings between adjacent molecules, which strongly depends on the molecular stacking mode such as the degree of π-orbital overlaps, the π–π stacking distance, and intermolecular interactions.[34] According to the semiclassical theory formulated by Marcus to describe the charge transfer rate k_{ET}[49]:

$$k_{ET} = \frac{4\pi^2}{h} \frac{1}{\sqrt{4\pi k_B T \lambda}} t^2 \exp\left(-\frac{\lambda}{4k_B T}\right) \quad (1)$$

where t is the transfer integral, λ is the reorganization energy, T is the temperature, and h and k_B are the Planck and Boltzmann constants, respectively. This theoretical framework has been extensively applied in the exploration of the correlation of transfer integral and molecular structures.[50–52] Based on this theory, a large transfer integral seems to be of great benefit to the charge-transfer rate, and thereby a high hopping carrier mobility in organic semiconductors. It is predicted that large π–π stacking distance, big tilt angle, and even displacement along a molecule axis will lead to a significant reduction of the transfer integral because of the decay of intermolecular interactions and electronic coupling. Thus, appropriate molecular packing with optimal π-atomic-orbital overlap is the key point for efficient charge transport and hence high-mobility OSCSs.

It is apparent that a summary of the relevant packing motifs in OSCSs is necessary for the overall understanding of

molecular packing in the solid state, which falls into four typical types (Figure 1c–f).[34] The first is the classical herringbone packing motif without face-to-face overlap between neighboring molecules (Figure 1c). In this type, the charge-transport property is strongly determined by the aromatic edge-to-face interactions, and the carrier-transporting path is associated with the relative strength of transfer integrals. The second is the co-facial herringbone packing motif with face-to-face overlap between neighboring molecules (Figure 1d). The enhanced π–π overlap is favorable for charge transport around the adjacent molecules, making a 2D charge-transport framework possible. The third is the 1D lamellar packing motif, where the charges only hop along one direction along with the π–π stacking, probably yielding a 1D anisotropic electronic property (Figure 1e). The last type is the lamellar packing motif with 2D π–π stacking (Figure 1f). Large transfer integrals arising from the strong face-to-face interactions will facilitate 2D transport pathways. Of course, from the theoretical standpoint, the expected molecular packing mode for high-performance charge-carrier transport is lamellar packing, due to the strong intermolecular interactions for the enhanced transfer integrals and realization of ideal 2D-network charge transport. Tremendous research efforts focusing on modulating the molecular packing modes have been made, such as choosing a high-performance prototypical conjugated backbone, increasing the π-stacking overlap via substituent modification, and even capturing a 2D co-facial packing arrangement. However, to be honest, the highest carrier mobility of the organic semiconductors is still held by the herringbone packing motifs, whose representative molecules are pentacene and rubrene. The circumstance should be concerned that it is nearly impossible to accurately evaluate the charge-transport properties only from the intrinsic molecular packing mode while neglecting other outer impacts, such as molecular solid-state phases within the operating devices, the interface effect, and the actual testing conditions.

In brief, molecular stacking with weak molecular transition dipole interactions is favorable for high solid-state emission efficiency, while strong intermolecular interactions and maximized π-orbital overlap are beneficial for efficient charge-carrier transport and high carrier mobility. It is apparent that one cannot have it both ways due to the difficulty of realizing ideal J-aggregates in practice, whereas H-aggregates usually stack in herringbone or lamellar packing motifs. However, the actual molecular packing modes strongly rely on the molecular structures, such as the molecular conjugated backbones, substituent characteristics, and even subsequent crystal-growth processing conditions. Therefore, rationally modifying the molecular structures is crucial for realizing high-performance organic light-emitting semiconductor materials.

2.2. Charge-Transport Properties

It is proposed that OSCSs with highly ordered structures as well as minimal traps and defects provide a useful tool for revealing the charge-transport mechanism in organic semiconductors. They are commonly constructed from conjugated oligomers via weak noncovalent bonds, which make the charge-transport properties quite distinct to their inorganic counterparts. Since the 1960s, a series of theoretical and experimental studies has been carried out to evaluate the charge-carrier transport mechanisms based on OSCSs.[53–61] It is generally accepted that a term of band-like motion is responsible for the charge-carrier transport in bulk, ultrapure OSCSs at low temperature.

Time-of-flight (TOF) measurements established the benchmark for the charge-transport mechanisms in the early studies using bulk ultrapure OSCSs at low carrier density. This method was first introduced by Leblanc and Kepler using a pulsed laser to irradiate one side of the OSCS for the photogenerated charge carriers.[53,54] Then, the drift mobility of the carriers (μ) is driven in the presence of an applied electric field across the OSCS layer and can be expressed as

$$\mu = D^2 / V t_{\mathrm{tr}} \tag{2}$$

The carrier drift time (t_{tr}) is evaluated by monitoring the photocurrent, and V and D are the applied voltage and crystal thickness, respectively. By carrying out TOF experiments on naphthalene crystals, Karl et al. observed rapid growth of the carrier mobility with decreasing temperature and the strong dependence of the electric field (**Figure 2**a).[55] In the temperature range of 150–300 K, a power-law dependence of mobility on temperature was obtained for holes, $\mu \propto T^n$, with $n = -2.9$. Accordingly, the band-like transport mode is well suited for a consistent description of the observed dependences, and a similar trend is obtained with hole carriers, which confirms the band-like transport mode in bulk crystals at around room temperature.

Organic field-effect transistors (OFETs) serving as a versatile tool are constantly used to reveal charge-transport characteristics of organic semiconductor materials. A typical OFET device is constructed with four principal parts, including an active semiconductor layer, a dielectric insulating layer, a gate electrode, and a drain–source electrodes.[34,56] According to the different device structures, OFETs can be classified into four common types: bottom-gate/top-contact (BGTC), bottom-gate/bottom-contact (BGBC), top-gate/top-contact (TGTC), and top-gate/bottom contact (TGBC), as shown in Figure 2b. In an OSCS-based OFET, the OSCSs are placed to the drain–source electrodes and separated from the gate electrode by the dielectric insulating layer. The charge carriers will be injected into the OSCS layer across the drain–source electrodes and will accumulate at the interface between the OSCS and the insulator layers via a gate voltage. In particular, the accumulated charge carriers can be governed by varying the gate voltage, giving rise to a variation of the conductivity of OFETs. The operation scheme of the OSCS-based OFETs can be described by the following equations:

I. The linear region with $V_{\mathrm{DS}} < (V_{\mathrm{GS}} - V_{\mathrm{th}})$. The drain current ($I_{\mathrm{DS}}$) is defined as

$$I_{\mathrm{DS}} = \frac{W}{L} \mu C_{\mathrm{i}} \left(V_{\mathrm{GS}} - V_{\mathrm{th}} \right) V_{\mathrm{DS}} \tag{3}$$

II. The saturation region with $V_{\mathrm{DS}} \geq (V_{\mathrm{GS}} - V_{\mathrm{th}})$. The drain current is given by

$$I_{\mathrm{DS}} = \frac{W}{2L} \mu C_{\mathrm{i}} (V_{\mathrm{GS}} - V_{\mathrm{th}})^2 \tag{4}$$

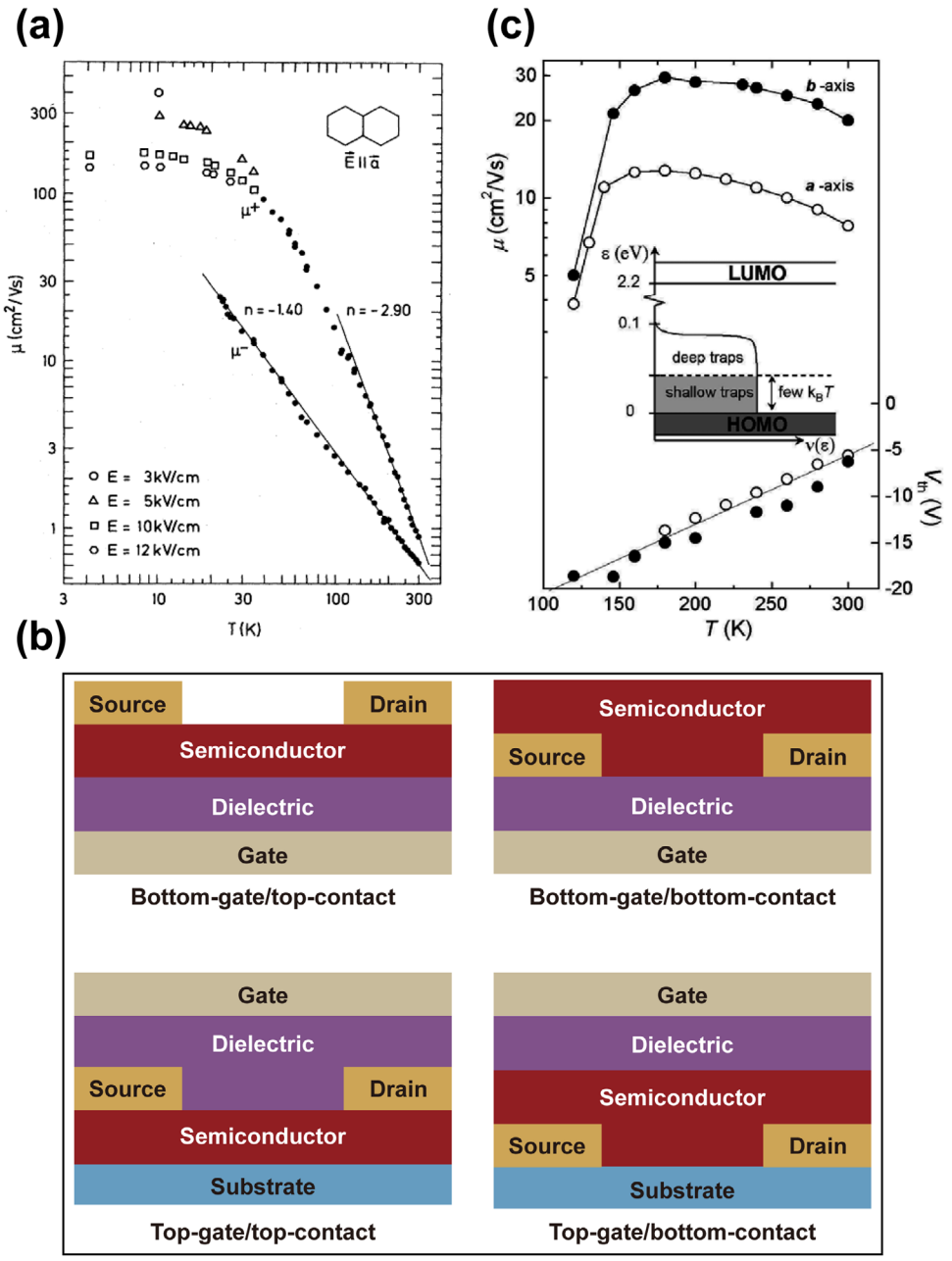

Figure 2. a) The temperature dependence of electron and hole mobility in ultrapure naphthalene crystal tested using TOF measurements. Reproduced with permission.[55] Copyright 1985, The American Physical Society. b) Four common configurations for OFETs based on OSCSs. c) Field-effect mobility and threshold voltage as a function of temperature examined on rubrene-crystal-based OFETs along the *a*- and *b*- axes. c) Reproduced with permission.[60] Copyright 2004, The American Physical Society.

In Equations (3) and (4), μ is the field-effect mobility of the OSCSs in the units of $cm^2\ V^{-1}\ s^{-1}$, C_i is the capacitance per unit area of the dielectric insulating layer, and L and W are the device channel length and width, respectively. The V_{th} is the threshold voltage, which can be derived from the plot of $(|I_{DS,\,sat}|)^{1/2}$ versus V_{GS} to $I_{DS} = 0$.

Particularly, charge transport in OFETs operates on the surface of organic semiconductors, where field-induced charges move along the interface between the organic layer and the dielectric insulating layer. It is suggested that the conducting channel is within no more than a few molecular layers (1–10 nm).[57–59] In this case, the density of field-induced carriers in OFETs may exceed that in bulk TOF experiments by many orders of magnitude. The developed OSCS-based OFETs without influences of grain boundaries, defects, and traps enable the observation of intrinsic transport of field-induced charges on organic surfaces.

Using a rubrene-crystal-based OFET with air as the dielectric layer, Podzorov et al. studied a temperature-dependence

intrinsic polaronic transport on the surface of rubrene crystals.[60] The intrinsic transport regime on the surface of organic semiconductors, that is, polaronic band-like transport was identified at high temperature (150–300 K), where the mobility increased with the decreasing temperature (Figure 2c). However, at lower temperatures (below 150 K), the mobility decreased exponentially with cooling, indicating that the charge transport is dominated by shallow traps that were probably induced by crystal defects like impurities, structural disorders, or surface states.

Hall conductivity measurements offer another alternative for the study of intrinsic transport on organic surfaces. The prominent advantage of Hall measurements is that the carrier density and mobility can be independently measured with a weak dependence on the contact resistance. The Hall carrier density n_H and the Hall mobility μ_H are evaluated as follows:

$$n_H = B\frac{I}{eU_H} \tag{5}$$

$$\mu_H = \frac{1}{B}\frac{U_H}{V}\left(\frac{L}{W}\right) \tag{6}$$

where the magnetic field is B, the four-probe voltage is V, and the Hall voltage is U_H. Typical dimensions of the structures are the channel width W, the distance between the voltage contact in four-probe L. Podzorov et al. reported the design of two types of OFETs based on rubrene OSCSs to study the Hall effect in the electric-field-induced accumulation layers on a crystal surface.[61] From the measurements, the Hall mobility was found to be an intrinsic, trap-free mobility, even if the charge transport is affected by the trapping. Due to the zero momentum (almost no Lorentz force), the charges trapped in the shallow traps do not contribute to the Hall effect, and the Hall mobility increases with decreasing temperature over the entire temperature range, which spans the intrinsic and trap-dominated conduction regimes. Therefore, charge transport on the surface of rubrene crystals occurs via delocalized states over the whole temperature (150–300 K), suggesting that the intrinsic charge transport is in fact band-like transport.

Undeniably, OSCSs embody the optimal electrical characteristics possible with organic materials due to their highly ordered structure and minimal defects. The charge-carrier mobility is one of the most important benchmarks for the performance of organic semiconductor materials. The mobility in the units of $cm^2\ V^{-1}\ s^{-1}$ is the proportionality constant between the magnitude of the applied electric field and the velocity working on a charge carrier, and largely determines the speed of an operating device. The first report on mobility was recorded based on ultrapure bulk anthracene OSCSs in TOF experiments, and they ranged about an order magnitude of 1 $cm^2\ V^{-1}\ s^{-1}$.[53] Also, the maximum mobility was found to be over 400 $cm^2\ V^{-1}\ s^{-1}$ in TOF measurements, which was obtained from naphthalene crystals at a lower temperature of 10 K.[55] Recently developed OSCS-based OFETs provide a powerful tool to investigate the field-effect mobility of organic semiconductors. Rubrene is one of the most representative semiconductor materials for OSCS-based OFETs, and it turns out to be highly compatible with device fabrication, building up a benchmark for the mobility values in all OFETs. It is noteworthy that the performance of OFETs deeply relies on the interactions between the semiconductor, gate dielectric, and electrodes. In particular, carrier trapping, charge doping, molecular reorientation, and a range of possible effects normally occur on the interface of semiconductor and dielectric layers to degrade device performance. To avoid these interactions, Rogers and coworkers fabricated an air-gap rubrene-based OFET with a thin free-space gap as the gate dielectric instead of the conventional solid dielectric layer to avoid any possible carrier traps, which exhibited extremely good mobility of about 13 $cm^2\ V^{-1}\ s^{-1}$.[62] Later, the application of novel double-gate transistors based on platelets of rubrene single crystals allowed the realization of the highest mobility of p-type carriers $\approx 43\ cm^2\ V^{-1}\ s^{-1}$.[63] This type of OFET consists of two gate dielectric layers: 9,10-diphenylanthracene single crystal and surface-passivated silicon oxide. By varying the gate voltages, the field-effect carriers can freely distribute inside the organic semiconductor layer, endowing the device with highly mobile carriers. The room-temperature mobility of carriers in rubrene-based single-crystal OFETs exceeds ten times that measured in TOF experiments. Another typical material for OFETs is pentacene, which has been studied since the 1980s. The highest-mobility carrier transport performance can be captured at the interface between pentacene crystals and quinone layers, which reaches 30–40 $cm^2\ V^{-1}\ s^{-1}$.[64] This remarkable performance of OSCS-based OFETs contrasts sharply with organic thin-film transistors and is even comparable to that of amorphous silicon FETs.

In general, most organic semiconductors are p-type, and these are mainly dominated by hole carriers due to the intrinsic electron-donating nature of π-electrons on the molecular backbone. The lack of stable high-mobility n-type organic semiconductors has impeded the progress of organic integrated electronic applications. In order to tackle this problem, scientists attempt chemical modification of electron-withdrawing groups on molecular terminals based on typical molecular frameworks to produce n-type organic semiconductor materials. For example, acene molecules and oligothiophene derivatives modified by fluoro or fluoroalkyl substituents exhibit promising n-type performance.[65,66] Fullerene and its derivatives provide a novel molecular prototype for developing high-performance n-type materials, the mobility of which have been improved, approaching 11 $cm^2\ V^{-1}\ s^{-1}$ based on their single crystals through a droplet-pinned crystallization process.[67] However, the properties of these n-type materials still lag far behind the p-type counterparts giving some major challenges, such as low charge-carrier transport, ambient operation stability, poor solubility, and large barriers for electron injection. Thus, numerous effective molecular design strategies are still needed for the exploration of high-performance n-type organic semiconductors.

OSCSs, with their inherently low density of traps, are expected to realize ambipolar operation with relatively high mobility of both carrier types for potential EL applications. However, most OSCS-based OFETs show unipolar characteristics that are dominated by hole transport. This is in contrast to the findings obtained with photogenerated carriers containing both hole and electron transport in TOF measurements. One of the important key points for ambipolar operation is that there is an effective injection of both type of carriers, especially for electrons, from electrodes into the organic semiconductors. An important strategy for obtaining ambipolar transport in OSCSs is using materials with a slightly deeper LUMO level, allowing effective electron injection. OFETs based on an oligoPPV derivative named

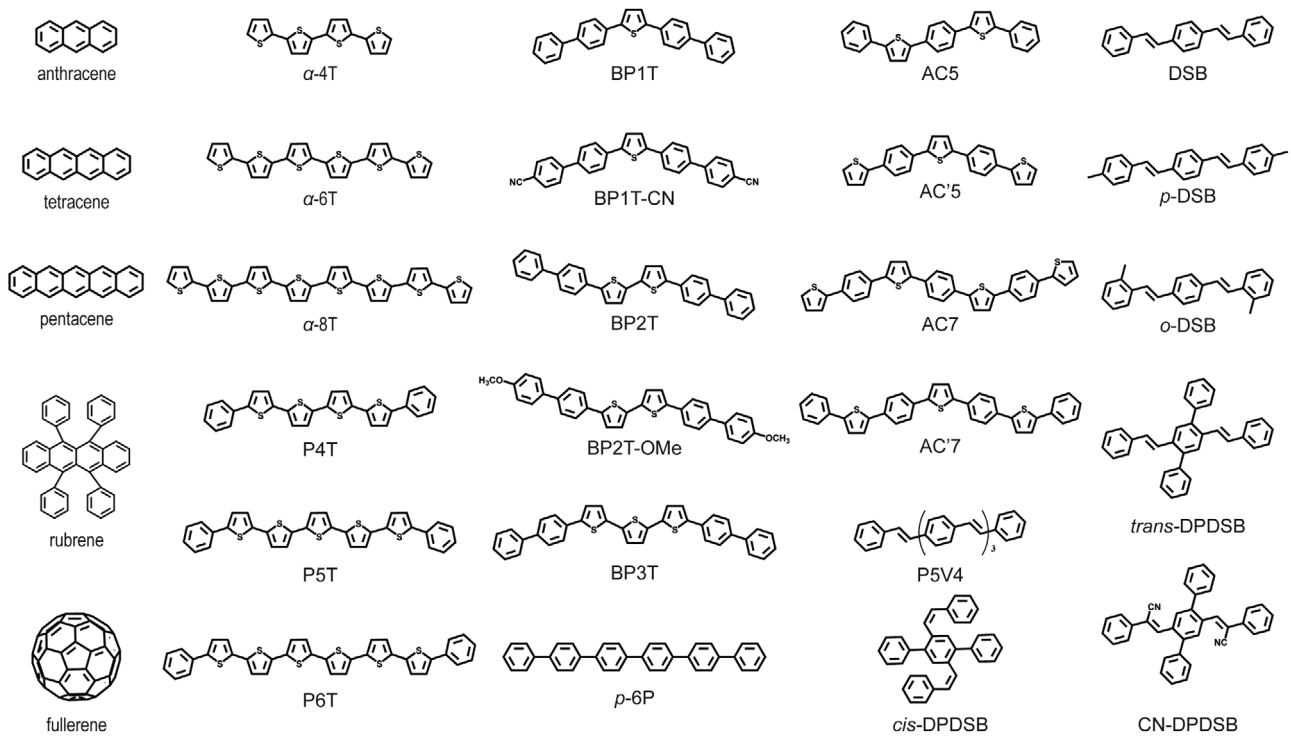

Scheme 1. Molecular structures of typical semiconductor materials.

p-bis(*p*-styrylstyryl)benzene (P5V4) with a 3.1 eV LUMO have been considered, and they exhibited obvious ambipolar operation.[68] It was proposed that the device operation mainly depends on the energy level alignment of the metal work function and the organic semiconductor HOMO and LUMO levels.[60] When the metal work function (Au or Ag metals) is close to the HOMO level, hole injection is apt to occur and induces the device's p-type operation. Conversely, n-type devices emerge when the metal work function approaches the LUMO. Ca is usually selected as a low-work-function metal to improve electron injection, despite its instability toward the ambient atmosphere. Therefore, an appropriate choice of electrode materials is very crucial for two-type carrier injection to obtain balanced ambipolar transport in OSCS-based devices.

2.3. Luminescence Properties

2.3.1. Molecules for Light-Emitting Crystals

An ideal conjugated backbone is a basic requirement for organic semiconductors containing both excellent carrier-transport characteristics and remarkable luminescence properties. The typical molecules, rubrene and pentacene, with recorded mobility in their crystals as exemplified above only satisfy the former requirement. High emission efficiency is difficult to achieve due to the luminescence quenching of luminophores at high concentrations. So as to address this issue, recently developed classes of materials fill a special optoelectronic niche, such as oligothiophenes, oligophenylene, oligophenylenevinylene, distyrylbenzene derivatives, and thiophene/phenylene co-oligomers (TPCOs), which manifest high luminescence quantum yields, stimulated emission, and even ASE in crystalline formation. ASE is a process related to lasing. In the absence of an external feedback structure, photons that are spontaneously emitted from a luminophore can still be amplified by stimulated emission while they interact with other excited luminophores during waveguide propagation in a gain material. To put it simply, intensive stimulated emission triggering an avalanche of photons is interpreted in terms of the ASE.

The ASE phenomenon was first observed from a monolithic α-linked oligothiophene single crystal, α-octithiophene (α-8T).[69] Molecular structures of typical semiconductor materials are shown in **Scheme 1**. The linear α-8T molecules have the quasi-planar all-*trans* conformation and are arranged with a herringbone crystal packing. Under optical pumping, low-threshold gain-narrowing, and dual-energy dependence of two distinct emission peaks are achieved. The gain-narrowed peak at 700 nm first appears at low pump energy with a linewidth of ≈8 nm full width at half maximum (FWHM), while the emission at 640 nm progressively emerges with increasing high pump energy. The two lines at 640 nm and 700 nm are in coincidence with the photoluminescence (PL) spectrum, which corresponds to the vibrational transitions. Similar phenomena have also been observed in α-quaterthiophene (α-4T) and α-sexithiophene (α-6T) OSCSs.[70–75] The corresponding two ASE emission peaks lie in 553 and 512 nm for α-4T and 645 and 595 nm for α-6T, respectively. Although strong stimulated emission and high mobility up to 0.1 $cm^2\ V^{-1}\ s^{-1}$ have been discovered in oligothiophenes, which are regarded as being able to bridge the gap between organic conjugated oligomers and organic lasers, however, the PL efficiency is still less than 9% measured for α-4T, α-6T, and α-8T

OSCSs. The origin is probably related to the strong intermolecular interactions in herringbone packing.[75]

In addition, oligophenylenes break the light-emission limit, extending the wavelength to ultraviolet and sustain high luminescence quantum yields in both solutions and solids as reported.[76–81] The representative *p*-sexiphenyl (*p*-6P) oligomer was widely investigated in needle-like crystals with a submilli meter length, which were epitaxially grown on the cleaved (001) face of a KCl substrate via vapor-deposition method.[76,77] Self-waveguiding amplification of blue light emission from the *p*-6P needle-like crystals with a narrowed spectrum at 427 nm was characterized as ASE. This self-waveguided emission was confined within the crystals and polarized parallel to the KCl surface based on the uniaxially oriented transition dipoles. The maximal emission intensity orientated parallel to the transition dipoles, and the minimum intensity was obtained along the vertical direction. This light emission was defined to be transverse-electric (TE) modes according to the arrangement of molecular axes parallel to the crystal plane.

The phenylenevinylene (PPV) molecular motif is one of the most widely known organic semiconductors because of the inspiration of the first organic solid-state laser based on MEH-PPV polymers.[82] Since then, its simple fragment, *trans*-1,4-distyrylbenzene (DSB), has become an impressive small-molecule emitter, with a relatively high luminescence quantum yield over 65% in crystal.[83] As molecular design has progresses, substituent effects on the basic of DSB molecular backbone are validated in practice, which reveals the correlation of structure and property. For instance, *para*- and *ortho*-methylated DSBs (*p*-DSB and *o*-DSB) are prepared to assess the impact of crystal packing on optical characteristics.[84] They are constructed in different crystal structures, which are orthorhombic for *p*-DSB and monolithic for *o*-DSB, while having the same ASE peak positioned at around 460 nm. Ma's group has also made a great progress over the past decade.[85–92] A twisted molecular configuration of 2,5-diphenly-1,4-distyrylbenzene (*cis*-DPDSB) was synthesized in order to weaken interdipole interactions in crystalline formation.[87] Also, they recently reported cyano-substituted oligo(*p*-phenylenevinylene) (CN-DPDSB) crystals with enhanced luminescence efficiency of about 95% due to the enlarged molecular distance by phenyl substituents.[85]

Another class of materials, TPCOs, targeting integration of excellent electronic and optical functionalities has been developed based on the hybridization of thiophene and phenylene at the molecular level. Over the past two decades, TPCOs have spawned many subsets including phenyl-capped oligothiophenes, block and alternating co-oligomers, and thienyl-capped oligophenylenes.[93–102] Among them, the various molecular backbones can be shaped into bent, zigzag, pseudo-straight, and bird's wing shapes, etc., which are propitious to weaken excitonic coupling and promote PL emission. Kanazawa et al. have demonstrated a rather high fluorescent quantum efficiency reaching 80% at 300 K in α,ω-di(biphenyl)-terthiophene (BP3T) crystals.[103] Another attractive feature of TPCO crystals is that the strong intermolecular interaction exerted through the herringbone packing assembles the molecules into a monolithic slab-like single crystal, where: i) the molecular long axes stand nearly upright against the wide crystal plane, and ii) the molecular transition dipole moments lie along the long axis of the molecules,

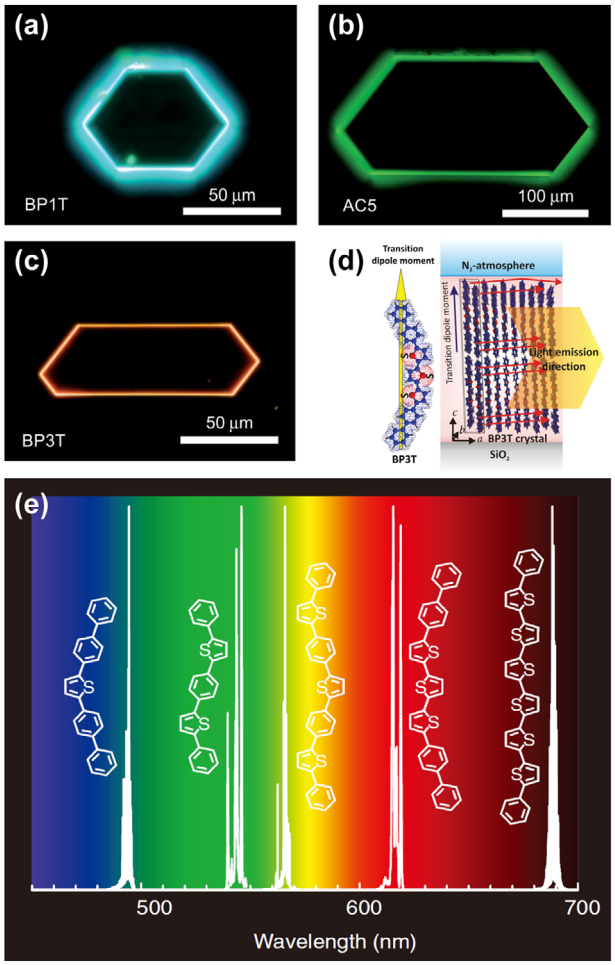

Figure 3. a–c) Fluorescence photographs of BP1T, AC5, and BP3T crystals under UV-light irradiation. a–c) Reproduced with permission.[27] Copyright 2011, The Royal Society of Chemistry. d) A schematic illustration of the self-waveguided edge-emission from BP3T crystal, where the molecules are stacked nearly upright to the crystal plane with their transition dipole moments parallel to the molecular long axis. Reproduced with permission.[102] Copyright 2009 Wiley-VCH. e) Spectra of typical laser oscillation from TPCO crystals with a desired full-color emission and their structural formulae. Reproduced with permission.[28] Copyright 2016, The Author, published by John Wiley & Sons on behalf of Society of Chemical Industry.

causing light emission in the direction perpendicular to the molecular long axis. This crystallographic structure endows the TPCOs with peculiar optoelectrical characteristics, such as high carrier mobility, ASE, and laser oscillation.[98,104–113] Owing to the molecular upright alignment, the light is efficiently confined inside the crystal and dominated at crystal edges. As shown in **Figure 3**a–d, obvious edge emissions contrast with the complete darkness interior of the crystal. Moreover, TPCO families provide a unique insight into the variation of backbone length and composition, which trigger the tuning of emission color over the whole visible range. Comparing 2,5-bis(4-biphenylyl)thiophene (BP1T) and 1,4-bis(5-phenylthiophen-2-yl)benzene (AC5), increasing the proportion of thiophene rings at a certain ring number induces a successive redshift of emission. For

constitutional isomers, BP3T with direct connection of the thiophene rings favors larger redshifts compared to the thiophenes and phenylenes alternating case 2,5-bis[4-(50-phenylthiophen-20-yl)phenyl]thiophene (AC'7).[30] Through mutually arranging the thiophenes and phenylenes within the molecules, the TPCOs can realize a desired full-color emission (as shown in Figure 3e).

Besides the diversity of molecular backbones, a novel concept of aggregation-induced enhanced emission (AIEE) is introduced for the design of efficient fluorescent materials in the solid state. These molecules usually possess twisted configurations with lower emission efficiency in solution, but high efficiency in the aggregate state. This phenomenon is attributed to the twisted geometry, which weakens molecular interdipole interaction and minimizes the likelihood of excimer formation in the crystal. Indeed, high emission efficiency and strong stimulated emission have been observed in AIEE OSCSs.[114–116] Another distinctive strategy to tailor the optoelectrical properties of OSCSs is molecular doping, in which small-molecule donor crystals doped with appropriate luminophores are used, acting as acceptors for the originally re-created exciton. Wang et al. demonstrated that they have ever exploited molecular doping in pure DSB crystals.[117] The improved crystal growth method allowed the incorporation of tetracene or pentacene into the crystals at high concentration reaching 10%. After doping, the emission shifted to the green and the red spectrum with luminescence quantum yields of 74% and 28% for tetracene and pentacene, respectively. Since then, different host and guest molecules have been tried out, such as P5V4 and BP3T, *p*-DSB and tetracene (or pentacene), anthracene and tetracene.[118–121] The appearances including spectrally narrowed emission, color-tunable emission, and improved external EL quantum efficiency for light-emitting devices, demonstrate the great potential of doped OSCSs for use in a wide variety of high-performance optoelectronic applications.

2.3.2. Lasing Features from OSCSs

OSCSs have been recognized as the most promising candidate for the application of electrically pumped organic lasers because of their superior optoelectronic gain properties. Apart from organic gain media, an optical feedback structure remains an essential prerequisite for such an application.[31] In some cases, the gain media itself is supplied with an optical resonator that provides sufficiently optical feedback. The most prominent is OSCSs whose coplanar crystal facets can constitute intrinsic Fabry–Pérot (F–P) resonators. The crystal facets work as reflective mirrors with optically high flatness, which guarantees strong self-cavity optical confinement in the crystal. Based on this structure, the lasing oscillation was first discovered by Ichikawa et al. in monolithic 5,5‴″-diphenyl-2,2′:5′,2″:5″,2‴:5‴,2⁗:5⁗,2⁗′-sexithiophene (P6T) crystals with a couple of F–P resonators providing a 2D self-cavity optical confinement.[122] A progression of extremely narrow emission lines emerges at the wavelength around 689 nm with a limited FWHM (≈38 pm) of the individual sharp lines in an interval of 121 pm. By analyzing the spectroscopic characteristics based on different sizes of crystals, the relationship between the mode intervals ($\Delta\lambda$) and resonator lengths (L) is clarified as below:

$$\Delta\lambda \propto \lambda^2/2L \tag{7}$$

where λ is the center wavelength of the lasing oscillation. The interval of the progressively structured emissions is inversely proportional to the resonation length.

After that, numerous OSCSs with well-defined polygons have been reported with the same phenomenon. Especially in TPCOs, their peculiar crystallographic structures are responsible for it, in which molecules stand nearly upright against the crystal plane giving rise to a parallel propagated light emission and subsequent edge emission.[99,110,123–128] Moreover, the regular molecular alignment induces a large optical gain along the direction parallel to the crystal plane, which is favorable for the amplification of propagated self-waveguided light between a pair of planar crystal facets. For example, 5,5′-bis(4′-methoxybiphenyl-4-yl)-2,2′-bithiophene (BP2T-OMe) crystal in orthorhombic form was reported with lasing oscillation appearing at 520–530 nm.[110] The lasing spectrum in **Figure 4** shows a series of narrowed modes resolved with a mode interval of 16 cm^{-1} and FWHM of about 4 cm^{-1} above the lasing threshold. A high net gain coefficient of 50 cm^{-1} was estimated, which is pertinent to the lasing oscillation. Another intriguing configuration of OSCSs for F–P resonators is based on their low-dimensional nanostructures, such as nanofibers or nanowires. In this arrangement, the nanostructures are integrated with optical waveguides and reflective mirrors at the same time. Since the emersion of stimulated emission in *p*-6P nanowire crystals, spectrally narrowed emission including random lasing and F–P modes lasing have been observed based on a number of designed 1D nanostructures.[129–131] Interestingly, a hollow rectangular optical microresonator based on tetra(4-pyridyl)porphyrin (H2TPyP)-RMTs crystal was recently developed with nearly 90° bending corners and submicrometer wall thicknesses.[131] A vibronic lasing action was interpreted to contain two kinds of cavity mode: one is the F–P mode oriented to the tube growth direction, and the other is the rectangular ring mode self-waveguided alongside sharp bends.

OSCSs with high thermal stability and relatively high melting points make them compatible with modern semiconductor processes. Therefore, other types of optical feedback structures can be integrated into these OSCSs, such as distributed feedback (DFB) structures and whispering-gallery-mode (WGM) resonators. The DFB structures have become one of the most popular configurations for organic lasers since the early 2000s.[31] In these, light will get scattered by a periodic corrugation while propagating in a slab waveguided media, and then combine through constructive interference. When the period of the corrugations meets the requirement of Bragg scattering, the light in a certain wavelength can acquire optical feedback for laser action which should satisfy the Bragg expression[5]:

$$2n_{\text{eff}}\Lambda = m\lambda \tag{8}$$

where λ is the lasing wavelength, Λ is the periodicity of the corrugation, and m is the order of Bragg reflection. Here the n_{eff} is the effective refractive index of the waveguide, which reflects average refractive indices of the geometry.

The fabrication strategies are restricted in the case of OSCSs due to their fragile nature. However, numerous efforts have been devoted to building up DFB structures on crystals. Fang et al. have attempted the laser interference ablation method to engrave diffraction-grating structures directly on the

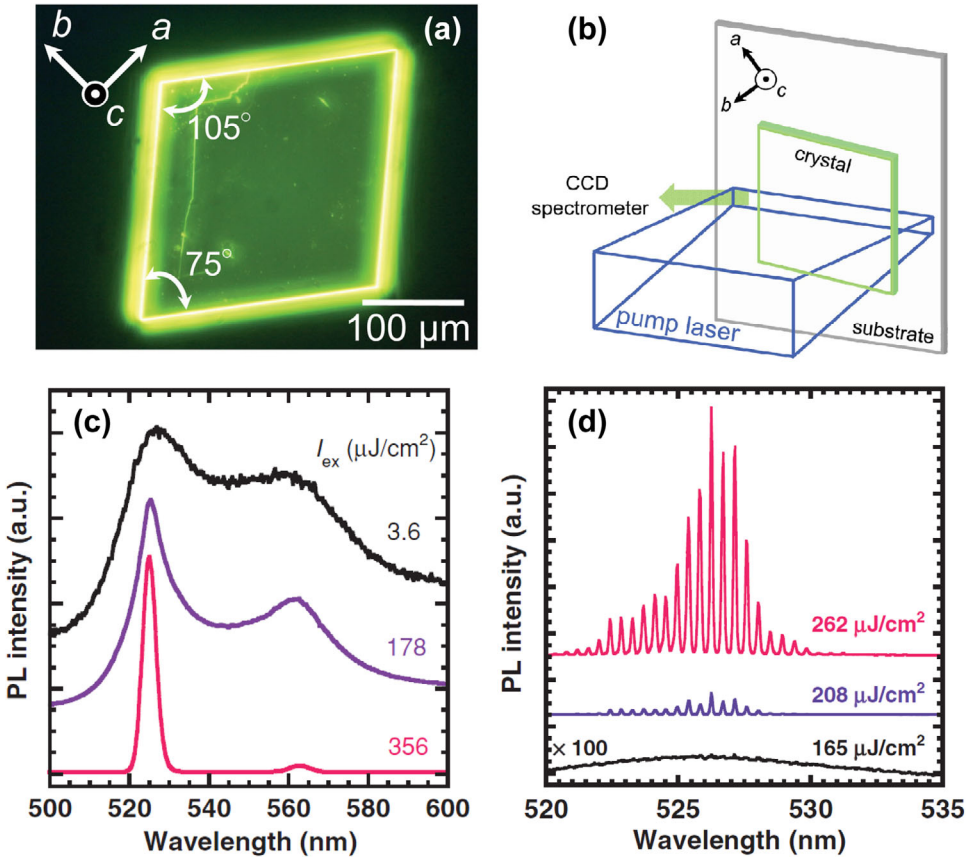

Figure 4. a) Fluorescence photograph of BP2T-OMe crystal under the UV light irradiation. b) Schematic diagram of the optical measurement with a stripe-shaped excitation beam irradiated on the crystal surface. c) PL spectra as a function of excitation density. d) Excitation density dependence of lasing oscillation spectra in the 0–1 band. a–d) Reproduced with permission.[110] Copyright 2012, Wiley-VCH.

2,5-bis(4-biphenyl)bithiophene (BP2T) crystal surface.[132] The crystals provide both gain medium and feedback structure. Obvious narrowed emission lines emerge at 565 nm with FWHM of 1.5 nm. The lasing threshold in DFB resonators is sufficiently reduced to be 25 μJ cm^{-2} compared to the ASE value of BP2T crystal. It is mentioned that the ablation process induces defects in the material, which will act as exciton traps. Therefore, the non-destructive laser interference lithography method was applied for OSCS-based DFB lasers.[133,134] External feedback structures are supplied by a corrugation of positive photoresist, which provides the optical feedback required for the OSCSs lasing. By replacing a plastic substrate, flexible DFB lasers based on OSCSs can be achieved with highly mechanical robustness. Recently, Hotta and co-workers focused on the focused ion beam (FIB) technique for the fabrication of the DFB-cavity structure.[135] Laterally emitted light occurring from the weak excitation was demonstrated with angle-dependence.

Another attractive optical feedback structure investigated frequently is WGM resonators, which utilize multiple total-internal reflections trapped within a sphere or ring of gain media with a large refractive index for lasing operation. OSCSs are ideally suited for this geometry, owing to their excellent optoelectrical performance, especially higher refractive index. Through complex semiconductor processes of photolithography and reactive-ion etching techniques, Fang et al. successfully realized micro-sized patterned disks and polygons based on slab BP1T and BP2T OSCSs.[136] Strong WGM lasing oscillation can be unambiguously observed from both circles and polygonal microdisks with lots of eigenmodes satisfying the condition of total internal bounce reflections at the microcavity walls (**Figure 5**). The large refractive index of the crystal (phase refractive index ≈ 2.9) and rather high *Q*-factor for microdisk cavity were also estimated according to the oscillating spectra. These results provide a new variable to consider in the quest for integrating photonic integrated circuits and enabling widespread applications.

2.4. Anisotropic Properties

In addition, OSCSs with well-defined molecular alignment inevitably confront structural anisotropy, which results in their anisotropic properties, and this is particularly the case with carrier transport and optical constants. As mentioned above, the intermolecular transfer integrals that significantly depend on the crystallographic direction are responsible for the anisotropic characteristic of the charge-carrier mobility. It is suggested that the largest transfer integral is along the direction with the strongest π–π overlap between adjacent molecules leading to the highest mobility. A pronounced anisotropy of mobility was first substantiated based on bulk oligomer crystals in TOF

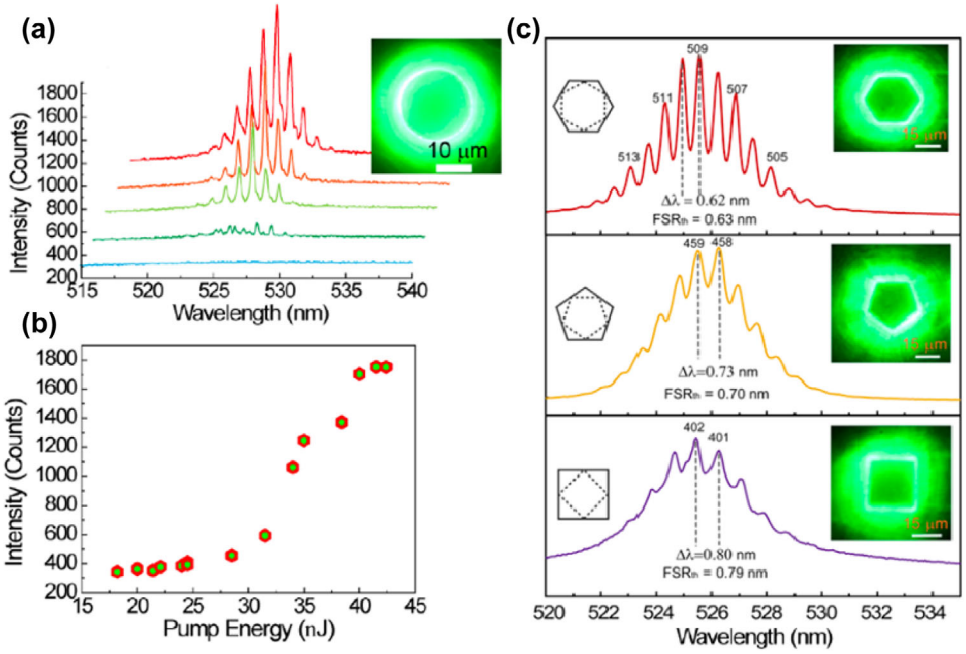

Figure 5. a) The WGM lasing spectra of a circle microdisk recorded at different pump energies. b) Superlinear dependence of the emitted intensity of one selected WGM lasing peak on the pump intensity for circle microdisk. c) Lasing spectra and images from polygon microdisk resonators. a–c) Reproduced with permission.[136] Copyright 2012, Wiley-VCH.

measurements.[55] Since the invention of OFETs, the exploration of field-effect charge transport on the surface of organic semiconductors has just been started. Rubrene crystals have served as a prototype to investigate the anisotropy of surface conductivity in different OSCS-based OFETs.[137] The representative work was the one carried out by Sundar et al. with lamination of rubrene crystals against a transistor stamp. In this work, the mobility was tested in the range of 360° by rotating the laminated crystal (**Figure 6**). The largest mobility variation happened along the crystallographic *a* and *b* axis by a ratio μ_b/μ_a of two. The cofacial orientation of molecules stacking along *b* axis facilitates the charge transport compared with the one along the other direction. In addition, a few crystals have been demonstrated with two- and even 3D charge-transport anisotropy.[138–140] The polymorphism of OSCSs provides a good platform for this investigation of 3D nature. This crystal phase transition can be ascribed to weak interactions between adjacent molecules and nonrigid structural properties. He et al. measured the 3D anisotropic mobility for OFETs for the first time by controlling the crystal growth conditions for suitable dimensions and orientation.[140] Two types of morphological crystals were used in this work, one a 2D hexagonal microplate, and the other with 2D microrods.

Another attractive anisotropic property related to crystal molecular arrangement is polarized emission. This feature is usually observed from linear conjugated molecules with uniaxially orientated packing in the crystals. The angle-dependent polarization of PL emission can be collected by rotating a linear polarizer. Normally, the emissions are strongly polarized along the molecular long axis, which corresponds to the orientation of transition dipoles. In addition, the maximum and minimum PL intensity are suggested to be along with two perpendicular polarization directions. The 1,4-bis(α-cyano-4-diphenylaminostyryl)-2,5-diphenyl benzene (CNDPASDB) crystals were recently reported to have uniaxial orientation.[86,141] The crystal structure revealed that all of the CNDPASDB molecules stack parallel to each other with an identical conformation and orientation in the crystal. The high polarization contrast of about 0.93 indicated a nearly linearly polarized emission. Moreover, the same phenomenon and even polarized spectrally narrowed emission have also been discovered in TPCO crystals as a consequence of their nearly upright configuration of molecules against the crystal plane.[76,142–144]

Additionally, the strongly anisotropic structures of OSCSs also rule their refractive indices in high anisotropy. Hotta and coworkers built up a scenario to determine the refractive index of an OSCS in its lasing oscillation wavenumbers. As the parallel crystal facets function as F–P resonators, quite narrow emission lines will be generated from the interference of intense forward and backward electromagnetic waves. The refractive index can be estimated on the basis of the mode intervals of the well-resolved longitudinal multimodes, according to the following expression[125,126,145,146]:

$$n = 1/2L\Delta\nu \tag{9}$$

where n is treated as the effective refractive index or group refractive index, L is the distance of the parallel crystal facets, and $\Delta\nu$ corresponds to the adjacent mode interval. The AC5 crystals in hexagonal configuration have ever been selected for the investigation of anisotropic refractive indices (**Figure 7**a–d).[125] These hexagonal crystals comprise three pairs of parallel facets along different lattice planes. After the crystals are photopumped with a thin laser stripe, longitudinal multimode lasing oscillations take place separately between the three parallel facets. The refractive

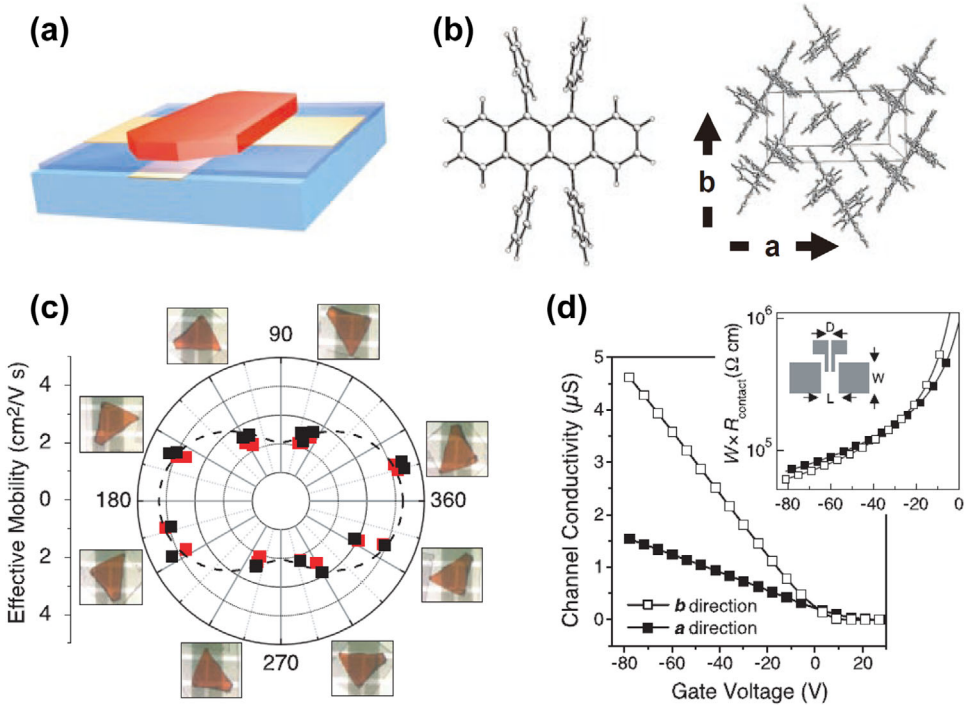

Figure 6. a) Schematic view of a rubrene-crystal-based OFET by lamination. b) Molecular and crystallographic structures of rubrene. c) Polar plot of mobility rotated at different angle directions of rubrene crystal. d) Four-probe conductivity as a function of gate voltage along the *b*- and *a*-axes of rubrene crystal. a–d) Reproduced with permission.[137] Copyright 2004, American Association for the Advancement of Science (AAAS).

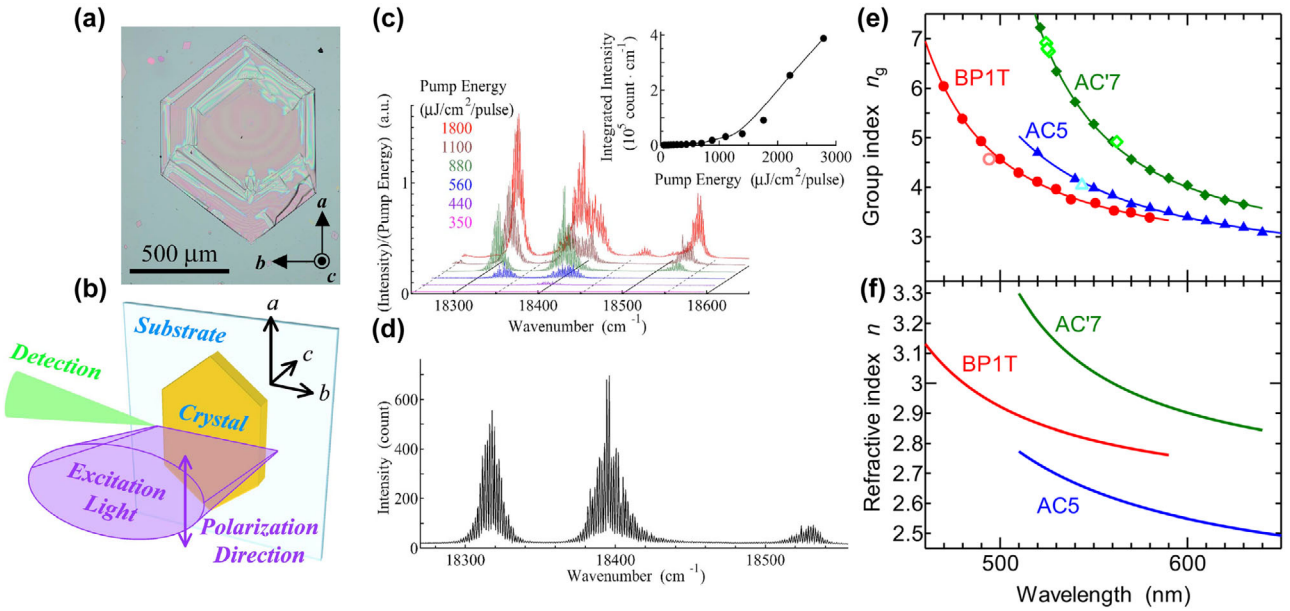

Figure 7. a) Image of a hexagon AC5 crystal. b) Schematic diagram of the optical measurement setup. c) Excitation density dependence of spectral profiles of the laser oscillation. The inset shows the correlation between the integrated emission intensity and pump energy. d) Spectral profile captured at an incident pump energy of 880 μJ cm^{-2} per pulse. a–d) Reproduced with permission.[125] Copyright 2008, American Institute of Physics. e) Wavelength dependence of the group refractive indices of the BP1T, AC5, and AC'7 crystals. f) Calculated dispersion curves of the phase refractive indices. e,f) Reproduced with permission.[145] Copyright 2011, American Institute of Physics.

indexes can be estimated from the three lattice planes, with an average value of 4.0. This refractive index is regarded as the value related to the direction perpendicular to the crystal bottom plane according to their highly polarized electromagnetic waves. As for the indices parallel to the crystal plane, polarized emission is measured on account of their molecular upright features. Then, anisotropic refractive indices along the three mutually orthogonal directions can be determined. The broadband PL spectrum allows the dispersion of group and phase refractive indices as a consequence of the wavelengths to be assessed by analyzing the fringe spacing over a wide range, as shown in Figure 7e,f, with various TPCO crystals. The OSCSs turned out to be anisotropic dielectric media with the relatively large refractive index leading to ease in light amplification, which renders them great candidates for organic solid-state lasers.

3. Crystal Growth Strategies for OSCSs

Owing to their desirable optoelectronic properties, high-quality organic single-crystalline materials are extensively required in optoelectrical functional devices. Unlike their inorganic counterparts, organic semiconductor materials have obvious advantages, such as low sublimation temperature and low melting point, which are convenient for low-temperature processing. Over the past few decades, tremendous progress has been made in developing strategies for crystal growth of OSCSs into highly ordered structures and with minimized impurities, which can be divided into three aspects, including the solution-processing method, the melt-recrystallization method, and the vapor-processing method.

3.1. Solution-Processing Method

Analogous to most crystal growth, the solution-processing method is the most typical and convenient method to prepare OSCSs. Most organic materials are soluble in common organic solvents, such as dichloromethane, chloroform, toluene, and tetrahydrofuran. This ensures some unstable large-molecular-weight materials can use their solubility for crystallization.[147] Solvent evaporation is one of the simplest ways to grow OSCSs in the liquid phase, and usually uses an oversaturated precursor solution containing an enormous amount of organic material. Following the slow evaporation of the solvent, the organic molecules precipitate to form nuclei and gradually grow into large crystals. This crystallization process basically relies on molecular self-assembly, which usually adopts typical noncovalent intermolecular interactions between neighboring molecules, such as hydrogen bonds, π–π stacking, and dipole–dipole interactions. However, in this method, it will consume extra time of about several days or even weeks to obtain large-size crystals. Alternatively, a fast method to obtain OSCSs is the slow-cooling method, where a hot or oversaturated solution cools down to the room temperature with crystal nuclei formation and consequent crystal growth. However, there is a prerequisite for the organic material, whose solubility is moderate at room temperature but changes considerably with temperature.

Besides these traditional crystal-growth methods, several novel smart approaches have been developed to grow high-quality OSCSs. Self-assembling submicrometer OSCSs can be performed through a solvent-exchange method in the liquid phase due to the strong intermolecular interactions (**Figure 8**a). The organic molecules are dissolved in a good solvent and then transferred into a poor solvent with limited solubility. The poor solvent makes a great contribution to this self-assembly process because of the minimum interaction between the material and the solvent. For example, self-assembled single-crystalline nanobelts of propoxyethyl-PTCDI can be grown based on this method using chloroform as the high-solubility solvent and methanol as the low-solubility solvent.[148,149] Another simple and fast method should be mentioned: the drop-casting method, that is, pouring a saturated precursor solution onto a substrate with gradual evaporation (Figure 8b). After that, the solution will reach oversaturation and induce nuclei formation and growth of large crystals due to self-assembly. This method was first tried by Mastorrent et al. and later extended to various organic semiconductors such as tetrathiafulvalene (TTF) derivatives and even some n-type materials.[150–153] The popularity of this method can be ascribed to the simple set-up that allows fine control over the processing factors, including solvent, concentration, and temperature, to obtain OSCSs with different morphologies. Another alternative is the dip-coating method which can grow microstructured OSCSs with aligned features. During the dip-coating process, a substrate is dipped into a precursor solvent and lifted out of the solvent at a controlled speed. Then continuous self-assembled microstructured OSCSs with the alignment of ordered arrays are obtained in the upward lift direction. Jang et al. produced self-aligned, highly crystalline soluble acene crystal arrays over large areas based on the dip-coating method, which exhibit excellent field-effect mobility on OFETs.[154] In particular, the shape and thickness of the formed microstructures can be changed under various conditions, including lifting speed, solution, and environment.

Alignment or patterning of self-assembled OSCSs is also investigated in the liquid phase, which is usually aided by external forces to guide the process, such as templates or wettability. Templates are used as a mold to print aligned and patterned OSCSs in the same framework of the template.[155] The main motivating force for the solution flow among the templates is the capillary force, which can control the position and orientation of the alignment/patterning of OSCSs. Elastomeric poly(dimethylsiloxane) (PDMS) with periodic structures is frequently employed as the template due to its ease of functionalization and molding. By a predeveloped PDMS stamp with defined 1D features, Cavallini and co-workers could achieve oriented, size-defined stripes of different types of organic semiconductors across the channel of the transistors to yield OFETs.[156,157] Meanwhile, substrate wettability has also been used to control the growth location of aligned/patterned OSCSs. A substrate surface treated with alkyl or fluoroalkyl groups exhibits a nonwettable property with poor solvent residual affinity, whereas those modified by phenyl groups display favorable surface for deposition of organic materials in the liquid phase. Optionally the substrate can be functionalized by various species of self-assembled monolayers (SAMs) such as 1,1,1,3,3,3-hexamethyldisilazane (HMDS), phenyltrichlorosilane (PTS), and

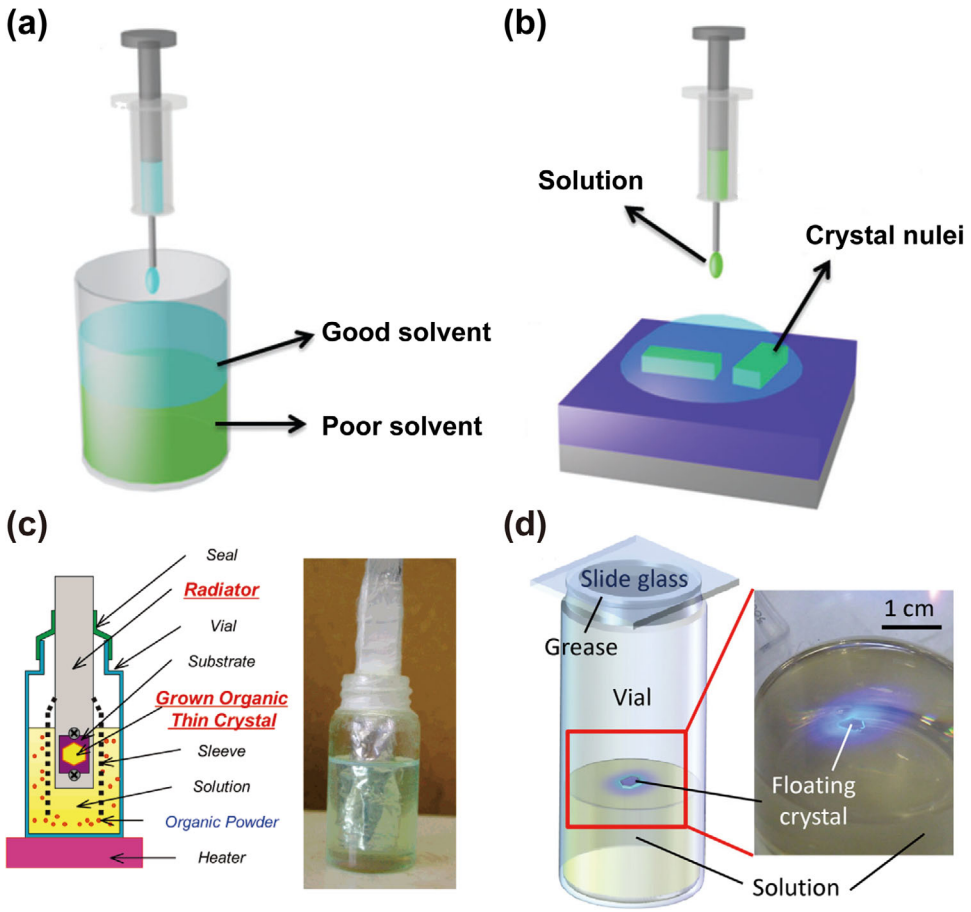

Figure 8. a) Schematic diagram of a typical solvent-exchange method by injecting good solvent onto the poor solvent. b) Schematic diagram of the drop-casting method by pouring a saturated precursor solution on substrates for crystal nuclei formation. a,b) Reproduced with permission.[25] Copyright 2017, The Royal Society of Chemistry. c) Schematic diagram and photograph of the liquid-phase-growth apparatus equipped with a thermal radiator. Reproduced with permission.[159] Copyright 2007, The American Chemical Society. d) Schematic diagram of a constant-volume decreasing-temperature method for crystal growth and an enlarged photograph of a fluorescent crystal floating on the solution. Reproduced with permission.[160] Copyright 2011, Elsevier B.V.

octadecyltrichlorosilane (OTS). Bao et al. demonstrated that they utilize a substrate with patterned wettability to produce patterning of aligned OSCS nanowire arrays.[158] The substrate was pretreated by OTS carried through a shadow-masked ultraviolet irradiation. During the process, aligned organic nanostructures were grown on the patterned wettable regions by controlling the shape and movement of the solution contact lines.

It is suggested that a straightforward way for device application is to adopt a monolithic single crystal. When monolithic crystal is obtained as a free-standing thin film, it is more convenient to be laminated on the surface of the device substrate. Yamao et al. recently designed an apparatus equipped with a thermal radiator to realize high-quality monolithic OSCSs in the liquid phase (Figure 8c).[159] With the help of the radiator, the silicon substrate could be cooled locally upon the radiator in the solvent. Then the organic materials spontaneously self-assembled onto the substrate through recrystallization and ended up as thin OSCSs with well-defined polygons adhering to the substrate. While exclusively choosing a silicon substrate with an oxide layer, the OSCSs on the substrate can directly serve for device construction, like OFETs. In order to precipitate large crystals in the liquid phase, they also tried an improved solution-processed method, named the constant-volume decreasing-temperature method (Figure 8d).[160] Based on this method, several crystal nuclei were selected and transferred into a preprepared low-oversaturated solution. Together with the growth of the nuclei, the solution became less oversaturated leading to a decrease of the driving force for the crystal growth. To continue the crystal growth, the low-oversaturated solution was kept by adding source powders. Finally, well-defined hexagon TPCOs crystals can be obtained with a large size of millimeters by applying this method.

For the solution-processing method, it is often the case that it is difficult to fully dissolve organic molecules with a long π-conjugated system in the solvent. In view of the kinetics of crystallization, the solvent molecules may also intercalate into the crystal lattice during the growth process. This detrimental effect will deviate the crystal lattice from its perfect crystal structure; thereby adversely influence the intrinsic optoelectronic and physiochemical properties.[32]

3.2. Melt-Recrystallization Method

Another strategy is the melt-recrystallization method, which is normally carried out by directly heating the organic materials to a certain temperature, and their subsequent recrystallization. Mostly, technology for recrystallization from melting requires organic materials possessing a well-defined melting point and high thermal stability.[147] This is not often the case with organic molecules, which usually have a strong tendency to evaporate or decompose during the melting process. In the early stage, conventional zone-melting methods (Bridgman, Stockbarger, and Czochralski methods) were sought for organic crystal growth, but they are suitable for only few materials due to the demand for low vapor pressure and ease in large quantity.[147] However, melt-recrystallization is having great developments over these two decades; among them, melting materials into desired device configurations for practical applications is the most attractive. Figi et al. have utilized melt-recrystallization, in which the liquid of the melted organic material flowed into predefined channels by capillary force and crystallized upon cooling.[161–163] This method can give rise to the fabrication of high-quality electrooptic organic single-crystalline devices, such as optical waveguides, phase modulators, and microring resonators. After that, the melt-recrystallization method was applied to various conjugated semiconductor oligomers such as *p*-*n*P (n = 4–6), anthracene, BP1T, and AC5.[98,164] The melt-recrystallized materials maintained highly ordered molecular alignments, and therefore exhibited good photoluminescent characteristics. Thanks to the high photoexcited emission yields and ASE properties of TPCO, BP1T was selected to construct microdisk and microring cavities for lasers by using electron-beam lithography and melt-recrystallization.[165,166] These microdisks and microrings presented obvious lasing emission in WGM and reduced lasing threshold, which was ascribed to WGM confinement in the narrow waveguide. Recently, Adachi et al. demonstrated an improved melt-processing method to prepare single-crystal films based on an oligo(*p*-phenylene vinylene) derivative substituted at both ends with pyrene moieties. By accurate control of the melting temperature, the recrystallization of the compound enabled the formation of large single-crystal monodomains in thin films, which exhibited a substantial enhancement of both charge-carrier mobility and photophysical properties.[167]

This melt-recrystallization method was further elaborated by Bi et al. in such a way that growth of Alq_3 nano/microcrystals was carried out aided by using a piece of double-filmed equipment where two Alq_3 films were stacked together and horizontally placed into a small chamber under a nitrogen atmosphere.[168] This equipment could sufficiently suppress the evaporation of Alq_3 molecules at high temperature. After being placed inside a sand bath and heated for 45 min, Alq_3 nano/microcrystals could be controllably obtained on the glass substrates (**Figure 9**a). To the researchers' surprise, the formation of Alq_3 nano/microcrystals could be changed from *mer*- to *fac*- with tunable color emission by increasing the melting temperature. Despite recrystallization, melting can lead to a change of crystalline phase. The same phenomenon was also observed from other organic materials whose molecules can form different luminescent polymorphs by tuning the molecular assembly structures in crystals through the melting process.[169,170]

In addition, this method is expected to complement other complicated industrial processes for the fabrication of functional electronic devices. Inoue et al. demonstrated that they integrated a thermal pressing method with melt-recrystallization to fabrication OFETs on a plastic film.[171] The semiconductor material with a low melting point could be melted and compressed with pressure to gain a thin active layer. This process proceeded at around the melting point without chemical reaction of the material. The final flexible OFETs showed good transistor performance and structural bending stability. Moreover, high-performance OFETs with high-quality crystalline rubrene patterns could be realized by combining the melt-recrystallization and a lift-off process (Figure 9b).[172] During the melting process for the crystallization, a prepatterned PDMS stamp was used and pressed onto the rubrene film at high temperature. After removal of the PDMS stamp, crystalline rubrene wires with a submicrometer spatial resolution were maintained on the substrate. OFETs made of the rubrene submicrometer wires exhibited saturation mobilities of as high as 4.5 $cm^2\ V^{-1}\ s^{-1}$ at ambient conditions. Therefore, this solvent-free method demonstrates great potential for simple and cost-effective fabrication of OSCSs for functional devices.

3.3. Vapor-Processing Method

In terms of the vapor-processing method, it is the most frequently used method for the growth of high-quality OSCSs. Most organic materials have sufficient vapor pressure and relatively low melting points, which ensures success in vapor-processing crystal growth. Additionally, there are no solvents or impurities involved in the vapor process. This makes the resulting crystals normally enjoy much better crystal quality than those produced from the solution-processing method.

After Karl first introduced the physical vapor transport (PVT) method to grow centimeter-sized anthracene OSCSs, Laudise et al. constructed a more convenient and easily controllable horizontal apparatus for growth of OSCSs on its basis.[173,174] After that, this apparatus was expanded following the successful growth of high-quality oligothiophene, pentacene, copper phthalocyanine, and anthracene OSCSs. The variety of strategies based on the PVT method generally fall into two major systems: open systems and closed systems.[147] Briefly speaking, the open and closed systems include, respectively, an inert gas or a closed environment. In the open system, the inert gas functions not only as a carrier gas that transfers the organic molecules but also as a protective gas that prevents oxidation during the crystal-growth process. The source material is placed inside a horizontal glass tube in the region of higher temperature (Figure 9c-1). With the help of inert gas, the sublimated organic molecules can be transferred to a lower temperature region where the crystal growth occurs within a narrow temperature range, and the submitted molecules with high kinetic energy will incorporate into the crystal lattice by the intermolecular interactions during the crystallization process. The grown crystals are usually hanging inside the tube wall, which makes them much easier to extract for their practical application (Figure 9c-2). High-purity hydrogen, argon, and nitrogen gases are usually chosen as the gas agent.

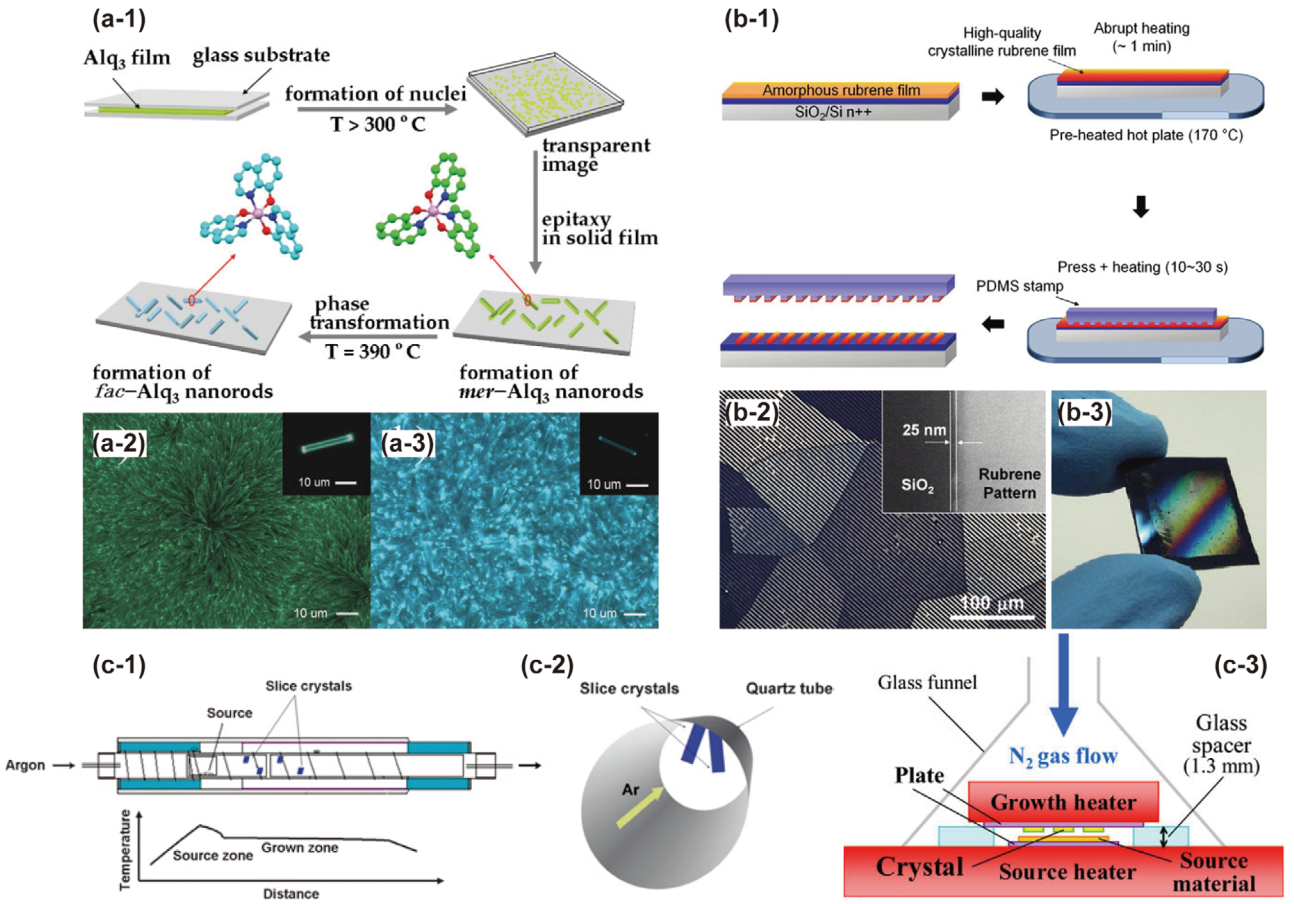

Figure 9. a-1) Schematic of fabrication process for preparation of *mer*-Alq_3 and *fac*-Alq_3 nano-/microcrystals by the melt-recrystallization method. a-2,a-3) Fluorescence microscopy photographs of *mer*-Alq_3 and *fac*-Alq_3 nano-/microcrystals, respectively. The inset is a clear view of one single microcrystal of each. a) Reproduced with permission.[168] Copyright 2010, Wiley-VCH. b-1) Schematic of PDMS lift-off fabrication process for an array of crystalline rubrene microwires by melt-recrystallization method. b-2,b-3) SEM and optical images of the array of crystalline rubrene microwires. b) Reproduced with permission.[172] Copyright 2011, American Chemical Society. c-1) Schematics of the conventional crystal growth apparatus by physical vapor transport method, and the temperature gradient. c-2) Schematic section view inside the quartz growth tube. c-3) Schematics of a unique crystal growth apparatus with a couple of vertical hot-plates by the physical-vapor-transport method. c-1,c-2) Reproduced with permission.[89] Copyright 2008, The Royal Society of Chemistry. c-3) Reproduced with permission.[175] Copyright 2009, Elsevier B.V.

By properly adjusting the gas flow, the sublimation, deposition, and crystal growth can be controlled accordingly, even achieving centimeter-sized crystals in several hours. In order to prepare high-quality crystals, the temperature gradient is suggested to be sufficiently small (about 5–10 °C cm^{-1}), and the sublimation temperature is set close to the melting point of the materials. For the closed system, the source materials are usually sealed inside an apparatus under vacuum or gas conditions. The growth can desirably be tuned by carefully regulating the growth temperature and controlling the gas pressure. Ichikawa et al. proposed a crystal-growth method based on a symmetric sealed glass tube that was placed on a uniformly heated hot plate.[105] The tube was evacuated and then filled with argon gas. The presence of the environmental gas will encourage the convective transfer of the molecules. By controlling the hot plate, the gas pressure and temperature of the tube can be suitably regulated. Under these conditions, molecules can be slowly transported from the bottom to the top of the tube by convection and consequently crystallize into fine crystals on the top of the tube. A serious of thiophene/phenylene co-oligomers OSCSs can be realized based on this method.

Some other modifications of the PVT method also play a key role in crystal growth. Yamao et al. reported a homemade apparatus that was constructed by a couple of vertical hot-plates in close proximity, within 1 mm (Figure 9c-3).[175] The narrow space surrounded by the hot-plates gives rise to crystal growth at the thermodynamic equilibrium. The lower plate was heated to sublime the source material, whereas the upper plate served as a receiving substrate. This crystal growth was routinely performed in an inert gas environment and the temperature of the lower plate was regulated to 5–10 °C higher than that of the upper plate, which ensured that the crystals would grow on the target substrate with well-defined polygons structure. If the substrate is changed to a silicon wafer covered with insulating silicon oxide, the resulting devices can directly be used for transistors. Taking consideration of the nucleation control, Yang et al. imported an inorganic adsorbent into the source materials to lower the sublimation temperature, slow the weight-loss process, and regulate the degree of

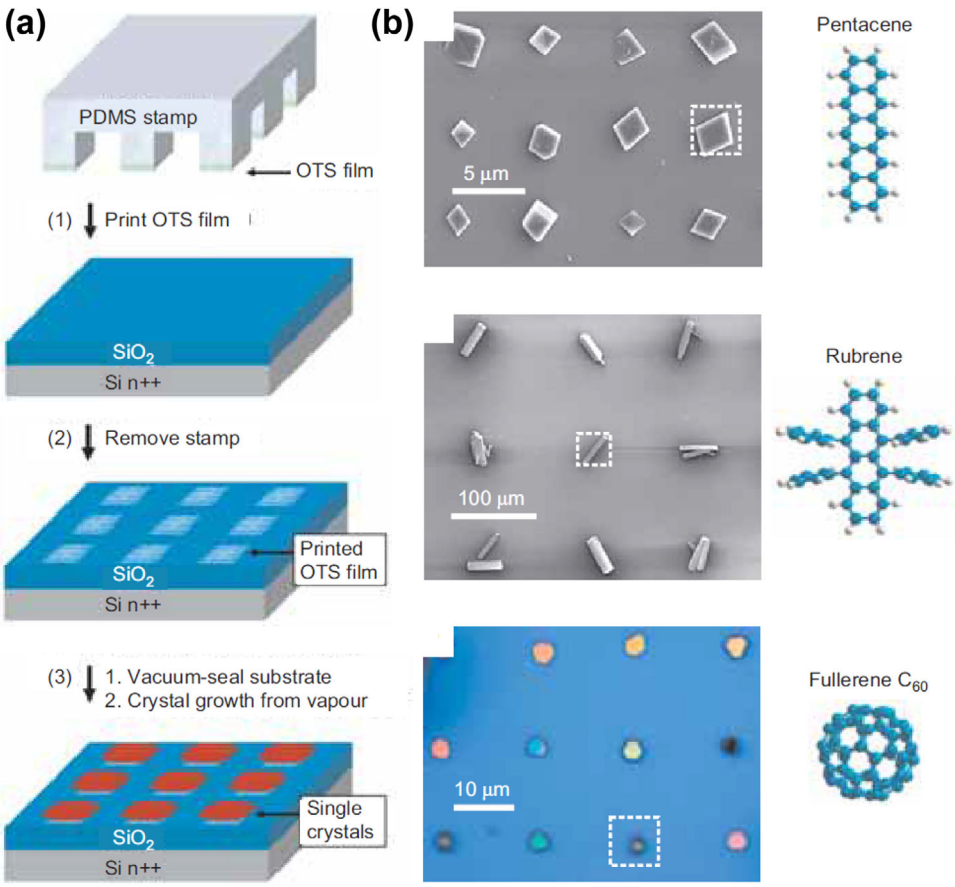

Figure 10. a) Schematic of fabrication process for preparation of patterned OSCS arrays by physical vapor transport method. b) Images of patterned OSCS arrays of different materials (pentacene, rubrene, and fullerene C_{60}). a,b) Reproduced with permission.[177] Copyright 2006, Springer Nature.

molecular vapor saturation.[176] Large-size thin-film OSCS with high quality can be prepared by this improved PVT method. Recently, researchers also attempted using the molecular doping technique for crystal growth by the PVT method.[117–121] The guest molecules could be doped into the host crystals by reasonable material selection and appropriate growth conditions. Then the initial properties of the host crystals were changed according to the guest molecules, including color-emission, charge mobility, and crystal structure. Large arrays of OSCSs have also been fabricated via the PVT method, where a patterned octadecyltriethoxysilane (OTS)-stamped substrate was employed to control over the nucleation of vapor-grown OSCSs (**Figure 10**).[177] It is suggested that the restricted crystal nucleation at the OTS-stamped regions stems from the high roughness of the thick OTS films as well as the use of a rather high-temperature substrate. Over the last two decades, this PVT method has been applied to a wide range of conjugated semiconductor oligomers for preparing OSCSs with sizes of several millimeters to micrometers and of optically high transparency.

Another option for fabricating OSCSs is the vapor-deposition method, in which usually a heating process is used to produce a molecular vapor, and then the vapor directly deposits to a receiver for crystal growth. Early in 2001, by a combination of careful substrate preparation and surface energy control, single-crystalline pentacene thin films with about 0.1 mm grain sizes could be grown from a quartz crucible heated over 250 °C in an ultrahigh-vacuum environment.[178,179] Among organic semiconductors, pentacene stands out as a model molecule due to its ability to form well-ordered films. However, this method is not applicable to all organic materials, and normally forms amorphous organic thin films. In order to carry out assembly and alignment of OSCSs, templates or external forces are usually exploited to assist this crystal-growth process. For example, Al_2O_3 templates with a nanopore diameter of about 200 nm were used to fabricate rubrene nanowire arrays via the vapor-deposition method.[180] In a home-made furnace, rubrene powder was sandwiched between two Al_2O_3 templates, and then vaporized and directly smeared into the Al_2O_3 templates. The growth processes happened at 300 °C with an inert gas. After the removal of the Al_2O_3 template, homogeneous arraying single-crystalline rubrene nanowires were obtained with a diameter of around 200 nm. And Takeyama et al. also proposed a new vacuum vapor-deposition method with an ionic liquid, and demonstrated that single-crystalline pentacene can be easily grabbed.[181,182] In this process, pentacene was deposited at a low temperature directly into an ionic-liquid droplet, and nucleated in the ionic-liquid droplet to form plate-shaped crystals in the single-crystal phase. An adsorbent was also used in the vapor-deposition method. The mixture of Alq_3/absorbent was proposed for the fabrication of single-crystalline nanowires.[183] When heated to the deposition

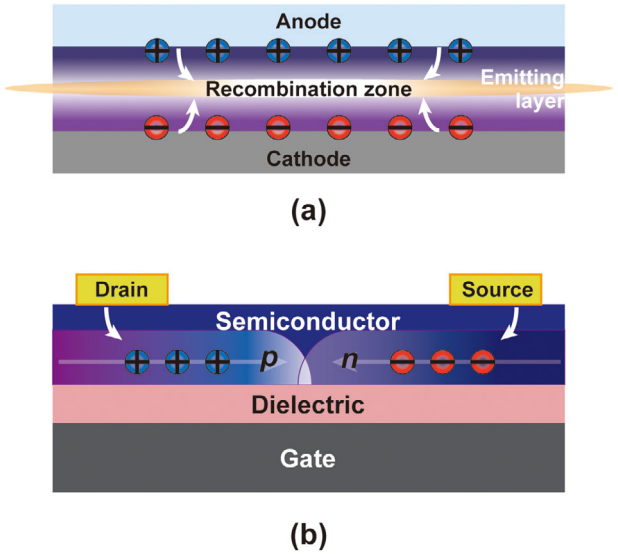

Figure 11. a) A schematic diagram of a conventional organic light-emitting diode (OLED). b) A schematic diagram of an ambipolar organic light-emitting transistor (OLET). a,b) Adapted with permission.[213] Copyright 2018, Wiley-VCH.

temperature, the Alq_3 sublimes to bring an appropriate degree of saturation via the adsorption–desorption equilibrium, which in turn results in the highly uniform formation of small Alq_3 crystal nuclei on the substrates. The subsequent Alq_3 vapor can be adsorbed onto the nuclei by intermolecular interactions, leading to the uniform growth of Alq_3 in 1D. Considering the molecular stacking interactions, 3D vertically aligned ribbon-like microstructured 2,7-dioctyl[1]benzothieno[3,2-b][1]benzothiophene (C8-BTBT) thin films can be achieved via an oblique-angle vapor-deposition method.[184] By varying the deposition angle, the C8-BTBT molecules tend to crystallize along the direction of intermolecular interactions, such as enhanced out-of-plane π–π stacking and van der Waals interactions. All these attempts exhibit that the vapor-processed method represents a promising entry for the fabrication of high-quality OSCSs, which guarantees better performance of the functional optoelectrical devices.

4. Light-Emitting Devices of OSCSs

4.1. Organic Light-Emitting Diodes

OLEDs have been developing rapidly over the past several decades, and a handful of product offerings are already on the market with remarkable performance, such as high luminous efficiency, low power consumption, fast response speed, and mechanical flexibility. A basic OLED consists of a thin organic compound layer that emits light in response to an electric current applied within two adjacent electrodes (**Figure 11**a). In general, amorphous/polycrystalline semiconductors are usually used for the emissive EL layer; however, they seem unable to tolerate high current densities as a result of their low charge carrier mobility, low purity, and massive carrier defects. OSCS materials have been identified as possible candidates for light-emitting operation due to their numerous advantages as mentioned above. However, reports on crystal-based OLEDs are fairly scant because of several existing problems that still limit the device performance.

Efforts have been devoted to applying OSCSs in OLED technology since 1963 by using bulk anthracene crystals.[37] The crystals were prepared by a primitive method with a thickness of more than 10 µm. Electroluminescence was only observed while the applied voltage reached up to 400 V, and the current density near the electrodes was reported to be about 100 µA cm^{-2}. These poor results failed to live up to expectations of OSCSs for organic lasers compared to their inorganic counterparts. The second report on crystal-based OLEDs was published after a long interval of about forty years, in 2002. Epitaxially oriented needle-like BP2T crystals grown on KCl substrates were used to construct an organic heterostructure by covering a *p*-6P layer which is beneficial for confining charge carriers confined in the low-dimensional structure with a narrow energy gap.[185] After depositing an Al cathode on one side, the device was wet-transferred onto indium tin oxide (ITO) glass as an anode. At low driving voltage, homogeneous blue light emission first emitted from the *p*-6P layer where the carrier recombination occurred. With an increase in voltage, the EL band shifted to green emission, corresponding to the BP2T needle crystals, which suggested that the combination region was confined inside the low-dimensional structures. However, the obtained EL pattern mismatched the crystal needle-like geometry, which can be ascribed to light scattering or imperfection of the interfacial contacts. Due to the different strategies for crystal growth, the morphology of the crystals, like size and thickness, is difficult to control. Yee et al. came out with an interesting idea wherein a microtome was used to slice a perylene crystal that was embedded in epoxy resin to less than 5 µm, which embedded in epoxy (**Figure 12**a).[186] Then the electrodes were thermally deposited on both sides of the exposed cross sections of the crystal slice, which constructed a sandwich-type device. Although an intense EL intensity and a high current quantum efficiency were obtained, the injection current density remained less than 0.4 A cm^{-2} and the present crystal thickness was still restricted by the microtome allowance (Figure 12b). Also, this method is not suitable for all kinds of crystals, whose fragile feature is the technological challenge for device fabrication.

Later, a typical method named the laminating method was attempted for the fabrication of crystal-based OLEDs. At first, a metal electrode with optimal work function was prepared on a clean substrate. Then a well-grown crystal was transferred to laminate onto the electrode and spontaneously bonded via a weak van der Waals force. Finally, another electrode was thermally deposited on the fixed crystal through a shadow mask. In the early work by Ichikawa et al., ambipolar transport was observed for BP3T-crystal-based OLEDs when Li/Al and Au were selected as the cathode and anode, respectively.[99] From the device, a maximum current density of 15 A cm^{-2} was achieved under continuous electric driving, which affirmed the tolerance of crystal-based devices for intense current driving. After that, this method was followed by other group members. A strong green-edge emission was obtained based on a high-performance 1,4-bis(2-cyano-2-phenylethenyl)benzene (BCPEB) crystal with a high PL quantum efficiency of 75% and mobility over 0.01 $cm^2\ V^{-1}\ s^{-1}$ for two-type carriers.[187] A special impact on the current–voltage characteristics was exhibited for crystal-based OLEDs with LiF/Al

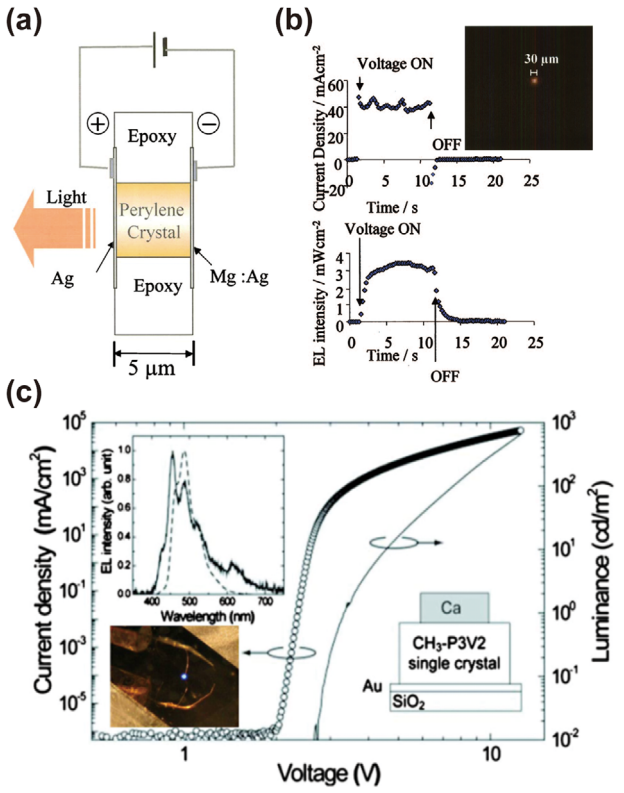

Figure 12. a) Schematic of perylene crystal-based OLEDs with crystal embedded in the epoxy. b) Response profile of injection current density and EL emission. The inset shows the EL emission of perylene-crystal-based OLEDs. a,b) Reproduced with permission.[186] Copyright 2006, American Institute of Physics. c) The current-density–voltage–luminance characteristics of *p*-DSB- (or CH_3-P3V2)-crystal-based OLEDs. Inset: PL of crystal, EL spectra, and light-emitting image of a crystal-based OLED. Reproduced with permission.[188] Copyright 2010, American Institute of Physics.

as the cathode in comparison to those with only an Al cathode, which suggests the importance of optimizing the energy levels between the organic crystalline semiconductors and the Fermi level of the metals. Then, an extremely low driving voltage of 2 V with a rapid increase in the current density was realized by engaging a *p*-DSB crystal with a thickness of only 240 nm (Figure 12c).[188] The thickness of the final crystal-based OLED was equal to the conventional thin-film OLED. A double-heterostructure crystal-based OLED was also achieved by adopting two stacked crystals, one p-type crystal and another n-type crystal, as the active emissive layer to balance hole and electron transport.[188] Although the total thickness of the heterostructured OLED was above 1.4 μm, a low onset of EL was observed at around 5 V with a maximum external quantum efficiency of about 0.025%. This value was almost one order of magnitude higher than that of the single-layered device, but still unacceptably low compared to thin-film devices. The poor contact via weak van der Waals forces between the electrodes and crystals was suggested as being the major problem for efficient carrier injection and this impedes the use of crystals for practical applications.

In order to address this issue, a smart technique of template stripping was carried out by Ding et al. in which the anode and cathode can be directly deposited onto either side of the crystals by thermal evaporation.[189] The schematics of the fabrication process on the basis of the template stripping technique are presented in **Figure 13**a. The OSCSs grown by PVT were transferred onto an OTS-modified Si/SiO_2 substrate (step 1). A thick Au anode was thermally deposited onto the crystals via a shadow mask (step 2). Then a droplet of photoresist polymer was drop-cast onto the device surface and compressed by a piece of glass (step 3). The polymer will spread to the edges of the glass and finally cover the whole device (step 4). After exposure to UV-light, the photoresist was cured and peeled off from the Si/SiO_2 substrate, so that the device could be transferred to the glass substrate (step 5). In the end, the Ca/Ag cathode was evaporated onto the opposite side of the crystal (step 6). The compact contact between the crystal and the electrodes ensures an efficient and uniform carrier injection.

This technique was first tried using TPCO crystals with special emissive characteristics of strong light confinement and self-waveguided edge emission stemming from their nature of molecular upright alignment.[189,190] Homogeneous light-emission with sparkling stripes at the device edges was observed from both BP2T- and BP3T-crystal-based OLEDs, which emitted green and yellow-green light, respectively. By analyzing the obtained EL spectra, a giant polarization splitting was found by rotating a polarizer in front of the devices. The polarized EL spectra oriented parallel to the crystal *a*-axis or *b*-axis corresponded to TM or TE polarization, respectively, where the electric and magnetic components are perpendicular to the crystal *ab*-plane. It was suggested that this appearance originates from the anisotropic microcavity, which was established by sandwiching crystals between two metallic electrodes. The optical anisotropy endows the crystal with a birefringence along different crystal axes. For example, the anisotropic refractive indices of the BP3T crystal along the *a*-axis and *b*-axis are estimated to be 1.84 and 1.63, respectively. The big discrepancy of refractive indices enables BP3T-crystal-based OLEDs to have a larger polarization splitting between the TE and TM polarization. Then the color-tunable light-emission can be altered from yellow-green (without a polarizer) to green (TE mode), and yellow (TM mode). This mechanism was also clarified according to the angle-resolved and polarization-angle-resolved EL spectra which were in coincidence with the theoretical calculations by the transfer matrix method. The color-tunable polarized EL behavior from the crystal-based OLEDs paves the way for 3D displays.

However, the dominant edge emission from TPCO-crystal-based OLEDs results in a low external EL quantum efficiency of around 0.001%. The alternative, surface emission, is one of the most efficient ways to promote device performance. Here, *p*-DSB-crystal-based OLEDs exhibited a strong and homogeneous surface emission because of the inclined molecules with respect to the crystal plane.[189] A pretty strong blue emission can be observed from the whole active area, whereas the EL spectrum mismatched the PL one, which was ascribed to the microcavity constructed between the metallic electrodes as well. It was proposed that the resonant wavelength in this microcavity device is determined by the total optical length of the cavity, which corresponds to the thickness of the crystals. For the operating devices, the onset voltage of 14 V was still quite higher and unacceptable. Then double-layered crystal-based OLEDs with a molybdenum oxide (MoO_3) layer were introduced as an

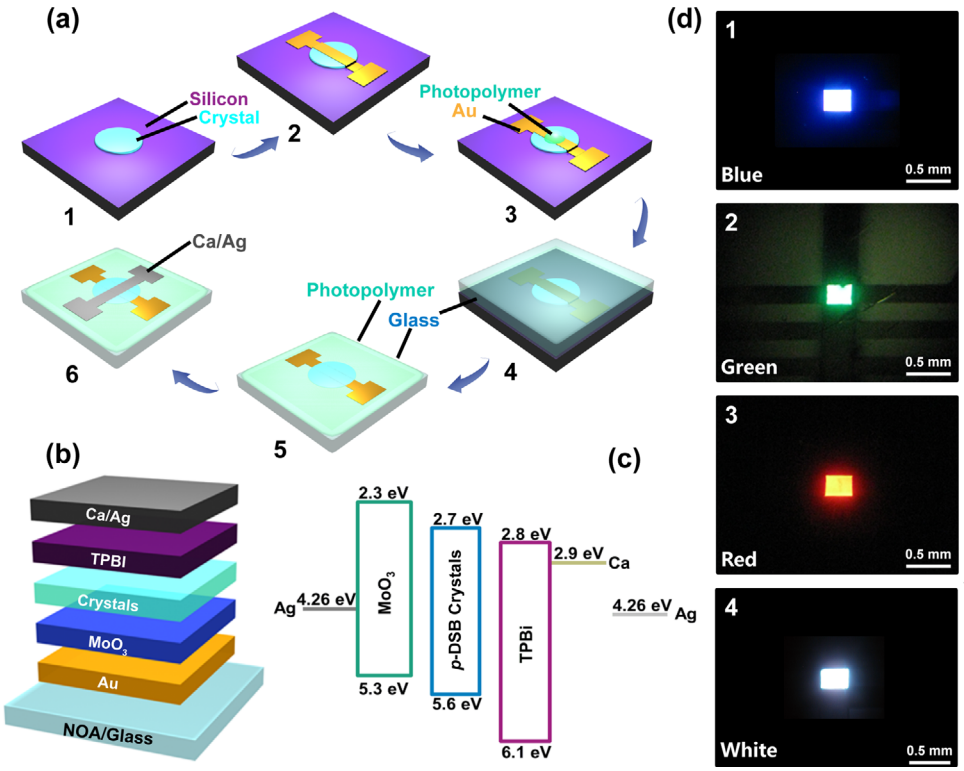

Figure 13. a) Schematic of the fabrication process of crystal-based OLEDs on the basis of the template-stripping technique. b) Schematic of the multilayered structure of crystal-based OLEDs. c) The energy level diagram of the multilayered device. a–c) Reproduced with permission.[192] Copyright 2017, Wiley-VCH. d) Photographs of the operating crystal-based OLEDs with different color emissions: 1) blue, 2) green, 3) red, and 4) white. d-1–d-3) Reproduced with permission.[192] Copyright 2017, Wiley-VCH. d-4) Reproduced with permission.[193] Copyright 2018, Wiley-VCH.

anodic buffer layer to lower the carrier-injection barrier.[191] As reported, the turn-on voltage of the AC5-crystal-based OLEDs decreased to 5 V, which was rather low and comparable with traditional amorphous thin-film devices. However, the balance of hole and electron injection and transport is the key issue for high-performance devices. Multilayered-structure crystal-based OLEDs containing one anodic buffer layer and another electron-transport layer constitute a major step toward balanced carrier injection and transport (Figure 13b).[192] MoO_3 with a HOMO level of 5.3 eV has been identified as a sufficient anodic buffer layer to further enhance the hole injection and modify the work function of the anodic metal layer. Moreover, the choice of materials for increasing electron transport is also very crucial, in particular, for conjugated semiconductors with a wide bandgap, so an obvious energy level mismatch between the electrodes and the LUMO level. The expectant material of 2,2′2″-(1,3,5-benzinetriyl)-tris(1-phenyl-1-H-benzimidazole) (TPBi) was usually used in conventional OLEDs, which works as both electron-transporting layer and hole-blocking layer. Then the multilayered-structure crystal-based OLEDs exhibit a remarkable performance by employing MoO_3 and TPBi as interface-modified materials to enhance carrier injection and improve charge carrier balance (Figure 13c). The thickness of the emissive layer is another important factor that influences the device performance.[192] As the thinner emissive layer leads to higher exciton recombination efficiency, the crystal should be grown as thin as possible, which is better for exciton confinement.

As mentioned above, the molecular-doping technique is able to tailor the optoelectrical properties of OSCSs. Tetracene and pentacene were chosen as dopant molecules in *p*-DSB crystals, which can change the original blue emission to pure green and red colors at a high doping concentration of 8%.[192] Besides the capability of turning colors, the dopant molecules can also act as electron- and hole-trapping sites for exciton recombination. Then, EL emission of three primary colors (RGB) was first observed from these crystal-based OLEDs with extremely high luminance and current efficiency of 820 cd cm^{-2} and 0.9 cd A^{-1} (Figure 13d-1–3). The efficient energy transfer from the donor *p*-DSB molecules to the tetracene and pentacene acceptors cannot be neglected for its contribution to the improvement in luminance and efficiency. Later, by precisely controlling the doping concentration of pentacene in *p*-DSB crystals, white emissive crystals were successfully realized with an equal PL intensity of blue and red emissive wavelengths. White-light-emitting crystal-based OLEDs built upon the multilayered structure were also demonstrated, with a maximum luminance and current efficiency of 1100 cd cm^{-2} and 0.91 cd A^{-1} based on these white crystals (Figure 13d-4).[193,194] The discovery of the substitutional doping mechanism was clarified by using polarized PL spectra measurement and first-principles calculations, which provided a microscopic picture of the stacking modes between the donor and acceptor molecules.[193] These results demonstrate the great potential of OSCS-based OLEDs for a wide practical application of high-performance organic optoelectronic devices.

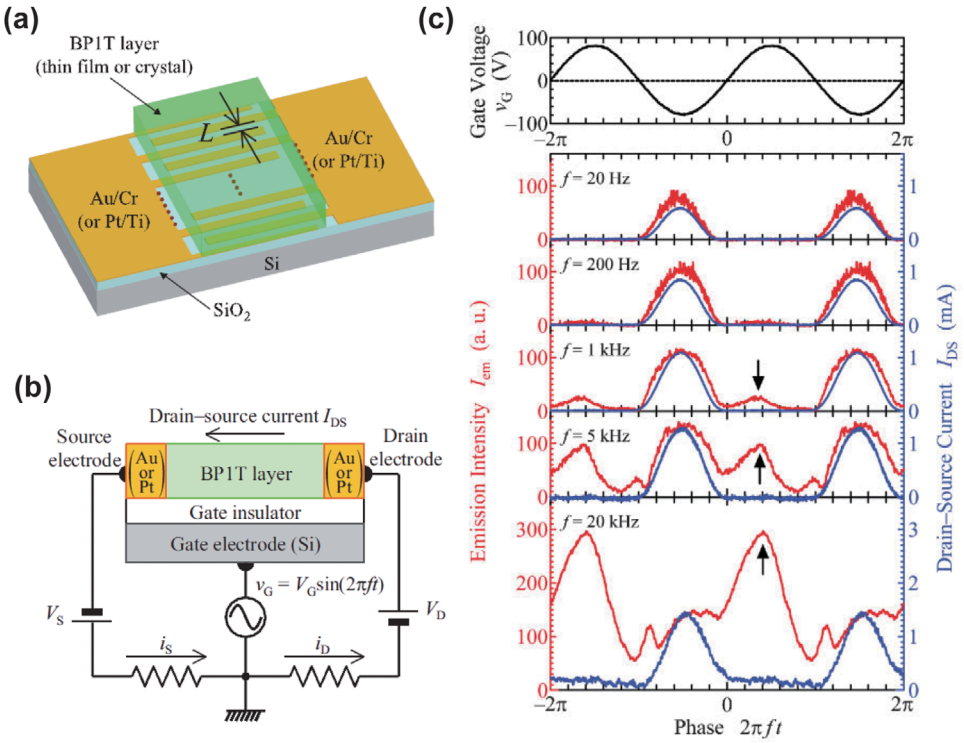

Figure 14. Alternating-current gate voltage (ACGV) operation of OLET. a) Schematic device structure. b) Schematic diagram of the electrical circuit. The drain and source electrodes are connected to DC power supplies. The gate electrode is connected to an AC power supply. c) Emission intensities of the device as a function of the gate-voltage phase. a–c) Reproduced with permission.[197] Copyright 2008, Wiley-VCH.

4.2. Organic Light-Emitting Transistors

Since the observation of laser oscillation in OSCSs, electrically pumped organic solid-state lasers based on these materials have been pursued in a novel field of optoelectronic devices, namely organic light-emitting field-effect transistors (Figure 11b). Their planar device geometry, embodying the integration of a luminous source and a processing switch, offers remarkable advantages over OLEDs. As the function of an OFET, the dielectric insulator acting as a capacitor offers a great capability of high current density in the semiconductor layer with high mobility, which is only proportional to the applied gate voltage. During the device operation, the gate voltage plays a vital role in controlling the carrier balance over the insulator/semiconductor interface for acquiring high exciton density. Furthermore, the varying gate voltage provides additional access to control the exciton recombination region in the active channel away from the metal electrodes. Therefore, the exciton-quenching process, pertinent to the device configuration, can be minimized. This behavior provides a strong probability for the quest of high emission efficiency, as well as light amplification in organic light-emitting devices.

After the first OLET was demonstrated based on the deposited tetracene film, plenty of organic semiconductors have been employed in this type of optoelectronic device for light emission.[195] Among them, OSCSs are particularly outstanding for their highly ordered alignment of molecules, which closely interact with one another, being responsible for the high carrier mobility.[196] Initially, the crystal-based OLETs were reported to operate in a typical unipolar mode where only holes accumulated and transported, forming a p-type conducting channel. The light is merely emitted at the interface between a crystal and one electrode where the combination occurs with poor electron injection. The induced carrier imbalance and exciton quenching at metal electrodes will seriously affect the consequent emission efficiency.

To avoid these apparent deficiencies, Yamao et al. put forward a novel method, named "alternating-current gate voltage" (ACGV) in which alternating-current voltages were applied to the gate electrode for promoting carrier injection from both drain and source electrodes, even though the device was in a symmetric metal electrode configuration with high work function.[197–199] A schematic of the operational principle of the BP1T-crystal-based OLET is shown in **Figure 14**a,b. This operation is supposed to start with a hole-dominated period in the conducting channel, which is in no pinch-off. As switching the gate bias polarity to positive, electrons are injected from the opposite electrode and the pinch-off sets in. Along with hole depletion, exciton recombination and light emission occur. The time-resolved spectra indicate that the emission is strongly related to the phase-resolved gate bias (Figure 14c). At low frequencies, the OLETs emitted light only at the negative gate bias with a blink-like emission. However, at high frequencies, another stronger continuous emission arose in the hole-depleting region while the gate bias swept from negative to positive. This ACGV method is attractive for its ability to inspect the detailed operation of the carrier injection and transport in organic semiconductors. When the sinusoidal wave gate bias was replaced by a square-wave bias, the emission intensity was increased by almost one order of magnitude.[199] By making use of a BP1T hexagonal crystal, a spectrally narrowed

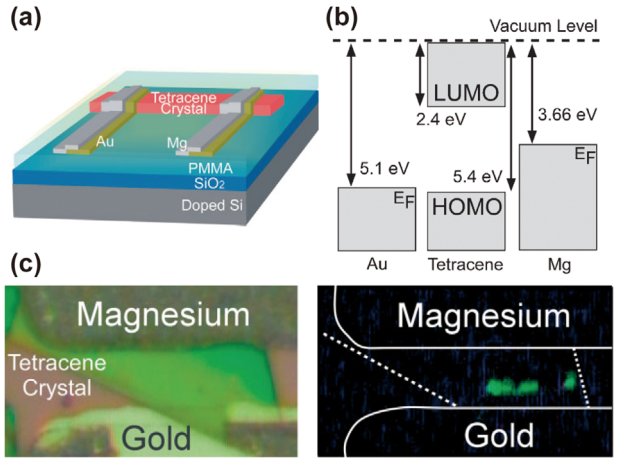

Figure 15. a) Schematic diagram of a tetracene-crystal-based OLET with asymmetric electrodes. b) Positions of the HOMO and LUMO levels of tetracene in relation to the work functions of gold and magnesium. c) Light-emitting images of a tetracene-single-crystal transistor under light and in the dark. a–c) Reproduced with permission.[200] Copyright 2007, Wiley-VCH.

emission was achieved with a spectral line at 491.5 nm and an FWHM of about 1.1 nm, which was probably associated with the laser oscillation in the crystal cavity.

Another feasible strategy is ambipolar charge transport, preferably with an asymmetric electrode configuration in OLETs. It is noteworthy to mention that the energy-level match between the Fermi level of the electrodes and the HOMO/LUMO levels of the organic semiconductors should be considered in the selection of metallic materials. Standard metals with high work function (Au or Ag) are used for hole injection, while low-work-function metals (Al, Mg/Ag, or Ca/Ag) are general for electron injection despite their instability toward the atmosphere. This work was initiated by Takahashi et al., who fabricated the first ambipolar OLETs based on tetracene crystals using Mg–Au asymmetrical electrodes (**Figure 15**).[200] Ambipolar operation and visible green-light emission was observed from tetracene-crystal-based devices. Shifting the recombination region along the conducting channel was also examined by varying the gate voltages. In this device configuration, the thin poly(methyl methacrylate) (PMMA) layer inserted between crystal and SiO_2 layers seems to play a significant role in the device performance. It is suggested that proper treatment with PMMA is a benefit to minimize electron traps and promote electron transport.[201] Also, a deeper investigation of these crystal-based OLETs reveals an absence of roll-off behavior in external EL quantum efficiency up to a current density in the several hundred A cm^{-2} range, while conventional OLEDs always have a roll-off before 1 A cm^{-2}.[202] Since then, these OLETs have risen to be a hotspot in the field of optoelectronic devices.

Upon this device configuration, many intriguing properties have been explored. For example, ambipolar operation with an apparent blue EL emission was observed from *p*-DSB-crystal-based OLETs in Ca–Au asymmetrical electrodes, demonstrating a nearly equal electron and hole mobility.[203] The promising laser medium of BP3T crystals was usually employed in ambipolar OLETs for their high-mobility values for holes (μ_h > 1 cm^2 V^{-1} s^{-1}) and electrons (μ_e > 1 cm^2 V^{-1} s^{-1}) with superior luminescence efficiency of up to 80% (**Figure 16**).[102] It is crucial for TPCO crystals that the molecular feature, standing nearly upright against the crystal plane, decides the principal directions of both the charge transport and light propagation, which coincides with the laterally spreading directions of the face-to-face molecular arrangement. Then, an intense light-confined edge emission with a polarization behavior and some signature of current-density-dependent spectral evolution can be observed from the TPCO-crystal-based OLETs.[100,102,112] Moreover, the recombination zone width is another important parameter of ambipolar OLETs, especially for display and lighting applications. During the measurements in various OSCS-based ambipolar OLETs, the recombination zone width is verified to be device-dependent, and it is proportional to the size of the area where there is no carrier accumulation in the vicinity of the recombination zone along with the transistor conducting channel.[204]

In addition, numerous strategies have been attempted to improve the device performance of these crystal-based OLETs. Kajiwara et al. designed a bilayer-crystal OFET with a p-type crystal and an n-type crystal constructing a p-n junction.[205] The two crystals of BP1T and 4-bis{5-[4-(trifluoromethyl)phenyl] thiophen-2-yl}benzene (AC5-CF_3) were laminated together on top of the gate insulator layer (**Figure 17**). This device, working under an AC-gate-bias operation, can supply excess holes and electrons from both p-type and n-type crystals, which gives rise to efficient recombination at the contact interface. As a consequence, brighter emission can be obtained with a maximum external EL quantum efficiency reaching 0.045%. In order to facilitate carrier injection, inserting a buffer layer between crystals and electrodes is a useful alternative. Metal oxides (like MoO_x) have been extensively investigated as a strong electron-accepting agent, which can significantly reduce the barrier for hole injection between the metal electrode and an organic layer without effects on carrier mobility. After introducing a MoO_x layer to ambipolar crystal-based OLETs, the formed highly conductive layer allows a high carrier density (>100 A cm^{-2}) in the recombination zone, resulting in excellent ambipolar operation.[68,206] A significant decrease of hole accumulation threshold voltage was reported in an OLET based on P5V4 crystals with an Au/MoO_x layer. A similar phenomenon was observed by the insertion of alkali halide CsF layer to BP3T-crystal-based OLETs with ease of electron injection.[207] Later, Yamada et al. proposed a novel OLET architecture where an aluminum-doped zinc oxide (AZO) layer was inserted between the crystal and the gate insulator. This metal oxide layer can offer an abundance of electrons, which assists the device with a large current density and an intense emission.[208] Molecular doping technology is also exploited to improve EL performance. OLETs based on tetracene-doped *p*-distyrylbenzene (P3V2) crystals revealed direct carrier recombination on the tetracene molecules, which can enhance the external EL quantum efficiency under ambipolar operation.[118] After that, BP3T-doped P5V4 crystals with evident ASE behavior were also used in OLET devices; nevertheless, no current-driven spectrally narrowed emission was attained.[119]

The aim to realize spectrally narrowed emissions in OLETs cannot do without the incorporation of resonators to improve

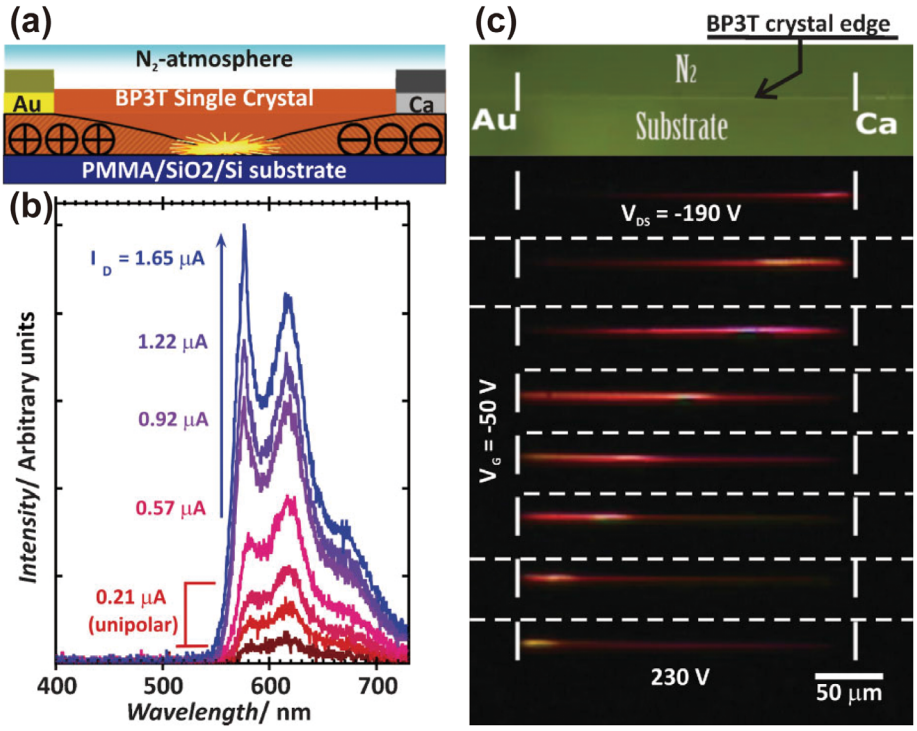

Figure 16. a) Schematic diagram of a BP3T-crystal-based OLET with asymmetric electrodes showing ambipolar light-emitting operation. b) Current-dependent spectral evolution of a BP3T-crystal-based OLET. c) Edge emission altered by drain voltage sweep under ambipolar operation of a BP3T-crystal-based OLET. a–c) Reproduced with permission.[102] Copyright 2009, Wiley-VCH.

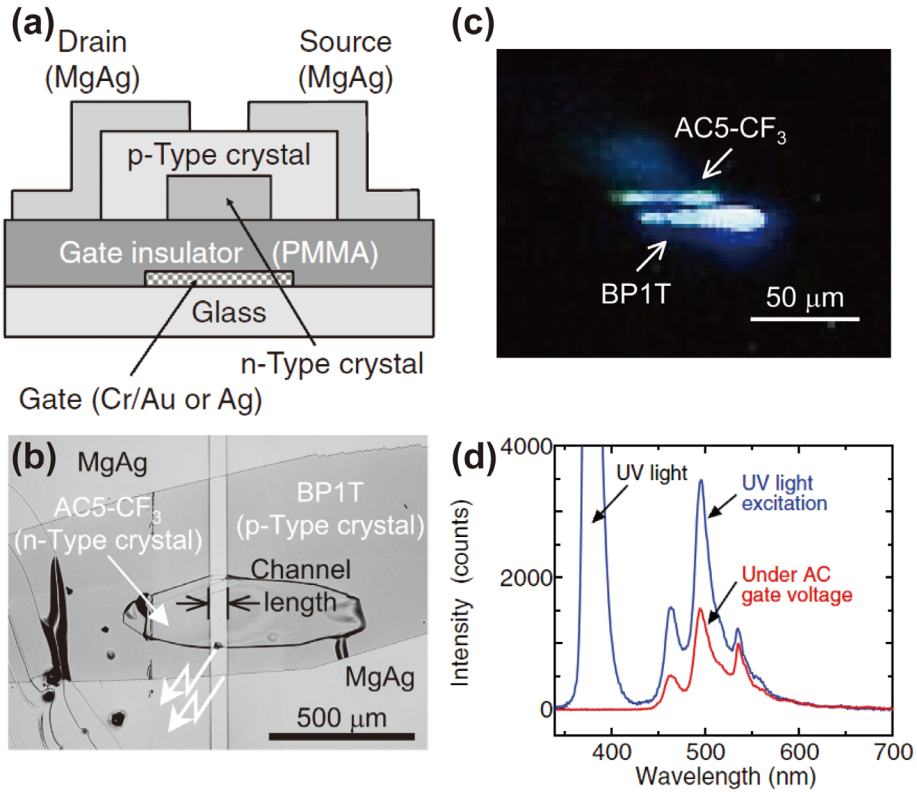

Figure 17. a) Schematic cross-sectional diagram of a bilayer-crystal-based OLET containing p- and n-type crystals. b) Top-view microscopy image of the bilayer-crystal-based OLET. c,d) Emission microscopy images and spectra of the bilayer-crystal-based OLET. a–d) Reproduced with permission.[205] Copyright 2011, Wiley-VCH.

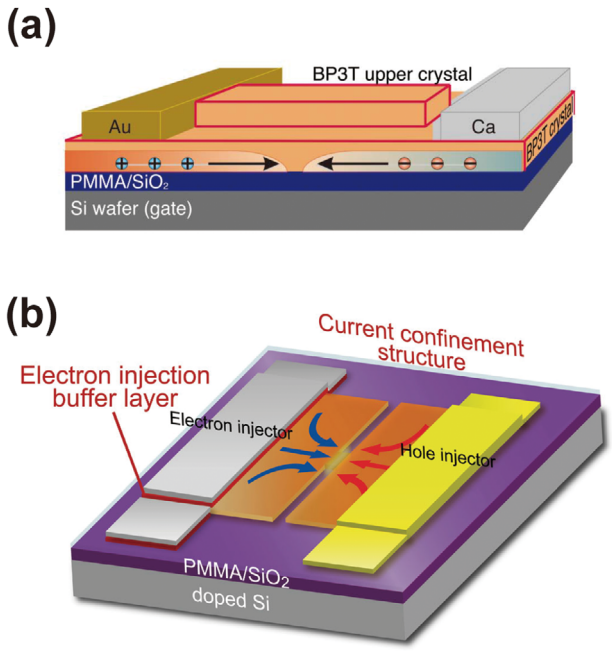

Figure 18. a) A schematic of a bilaminar BP3T-crystal-based OLET with a single-crystal optical feedback resonator. Reproduced with permission.[212] Copyright 2012, Springer Nature. b) A schematic of an improved BP3T-crystal-based OLET with a current-confinement structure by laser etching. Reproduced with permission.[207] Copyright 2012, Wiley-VCH.

the optical outcoupling of the emission. DFB structures are one of the most frequently used resonators for their compatibility with the fabrication of OLETs. Diffraction gratings can be integrated into different parts of the device via diverse manufacturing technology. Okada et al. nanoimprinted a 2D diffraction grating structure on photoresist polymer film working as the gate insulator, together with the SiO_2 layer.[209] The grating photoresist film comprises a triangular lattice of circular air holes which contributes much to the current-injected spectrally narrowed emissions with an FWHM down to 3.0 nm. Due to the strong self-waveguide effect of TPCO crystals, emissions tend to be propagated along the slab crystal plane. If a diffraction grating is located at the pathway of light propagation, a coupling between the waveguide and the DFB is expected. Recently, Yamao demonstrated a 2,5-bis[4-(5′-phenylthiophen-2′-yl)phenyl]thiophene (AC'7)-crystal-based OLET equipped with 1D diffraction-grating structure, aside from the conducting channel zone.[210] They engraved grating patterns on the surface of a SiO_2 insulation layer using a FIB apparatus. With the device operating under square-wave alternating gate voltages, current-injected spectrally narrowed emission was observed as a dominant line at 556.3 nm with an FWHM 2.05 nm. Another option is to fabricate the grating structure directly on the crystal surface. Maruyama et al. improved the soft ultraviolet-nanoimprint lithography method, which enabled 1D grating patterns on BP3T crystals.[211] Apparent resonant effects that stemmed from the gratings were observed in both PL and EL spectra.

Apart from the incorporation of diffraction gratings, an F–P cavity formed by the crystal parallel facets was recently loaded by Bisri et al., acting as a resonator to the OLETs.[212] Two BP3T crystals were laminated together, which looked like a couple, as shown in **Figure 18**a. In this structure, the upper crystal worked as a feedback resonator due to the parallel facets and the lower one supported as an active conducting channel in OLETs for exciton recombination. Then, the optical directional coupling can be realized due to the perfect self-waveguide characteristic of the BP3T crystals within the optical feedback resonator. This crystal system was verified to reduce the threshold energy for spectral narrowing and nonlinear intensity increment of the PL emission. When applied to the OLET device, a current-driven spectrally narrowed emission exhibiting a threshold tendency was successfully achieved. On the other hand, the current density is another important factor for electrically pumped lasers, which should be sufficient for lasing population-inversion in the semiconductor materials. In order to increase the current density, a current-confinement structure was adapted in the OLET devices in which the conducting channel parallel to the channel width was laser-etched with a small region (Figure 18b).[207] The confinement region was approximately two orders of magnitude smaller than the original, leading to an increment of current density with over 100 times. As a consequence of this structure, the light emission of the laser-etched BP3T-crystal-based OLETs was dramatically increased with a maximum value of current density estimated to be about 33 kA cm^{-2}. All of these aforementioned findings have demonstrated that crystal-based OLETs are a promising candidate to push the performance limit of organic light-emitting devices for an electrically pumped organic laser.

5. Conclusion and Outlook

Despite the recent tremendous progress made in OSCS materials and devices for light-emitting applications, there still remain challenges lying ahead for crystal-based light-emitting OLETs and OLEDs in order for commercialization. Over the past few years, different kinds of physicochemical approaches and synthesis strategies have been successfully developed to produce high-quality crystal materials. However, the performance of the OSCS-based light-emitting devices is still below that of the amorphous-materials-based organic devices. There are still a lot of problems rendering OSCS-based devices impractical for applications. Many efforts are still required to seek novel materials that possess better luminescence properties coexisting with remarkable carrier transport characteristics. Most currently available high-mobility OSCSs show weak or even no emission.[213] Therefore, the optimization of material optical properties is crucial for high-performance light-emitting devices. It is suggested to harness materials that generate more singlet excitons with a minimum path of triplet exciton creation. In addition, the utilization of an alternate in the triplet exciton state is probably a good option. Although the optimization of optical properties is ongoing all the time, the transport characteristics, especially balanced carrier transport, have not been improved with a sufficient research effort. For light-emitting devices, balanced hole and electron transport is most important for exciton formation and recombination, which is the key point for the device external quantum efficiency. Thus, the rational combination of high mobility and high optical properties by molecular design is necessary.

Although current organic light-emitting devices based on amorphous films are being adopted in industry, progress into OSCS-based devices has significantly lagged behind due to limitations in materials and device fabrication technology. Their intrinsic properties of fragility, softness, and solubility in organic solvents present an obstacle to device integration, especially incorporation with the high-resolution photolithography technique. In our previous work, a simple and nondestructive method of template stripping was applied to realize OSCS-based OLEDs with compact contact between crystal and electrodes and to obtain uniform light emission of devices.[189,190] This method not only solves the contact problem between the crystal and the electrodes, but also treats the crystal in a friendly way. Therefore, rational device fabrication technology needs to be significantly improved for high-integration industrial applications.

The stacking mode plays a pivotal role on the performance of the crystals themselves on the impact of strong intermolecular interactions. A deeper understanding of the molecular arrangement dealing with crystal engineering is beneficial for molecule design and synthesis guidance. Chemical modification by introducing appropriate substituents is an effective way to not only change the nature of molecules but also control the molecular alignment. For example, the 2,5-bis(40-cyanobiphenyl-4-yl)thiophene (BP1T-CN) crystal, whose molecules are aligned in a horizontal direction to the bottom crystal plane, is a promising candidate for light-emitting devices with evident surface emission.[26,27]

Although there are continued advances in crystal-growth strategies, a strategy for controllable crystal thickness and surface area is still lacking. The crystal thickness is limited to be above tens of nanometers, which cannot reach the expectations for light-emitting devices compared to the conventional ones based on amorphous materials. Moreover, it is worth noting that the performance of a device is indispensable with the thickness, which will strongly influence the device threshold and efficiency. On the other hand, large-area crystals are essential for practical industrial applications, such as patterned crystal-based OLETs and OLED device arrays for achieving large areas of display and illumination. As was mentioned above, all three crystal-growth methods have the potential for the development of large-area crystals. However, to date, the research on this field is slow going, and there remain some challenges.[25,32] In the solution-processing method, if the material in-plane intermolecular interactions are much stronger than the out-of-plane ones, it is possible to self-assemble the molecules into large-area crystals due to the strong dominating intermolecular interactions. To produce large-area crystals from solution, it is necessary to decrease the crystallization speed so that a self-assembly process can be achieved. However, this usually requires a time-consuming process, which may take several days, weeks, or even months, depending on the type of materials. The melt-recrystallization method is believed to be the most convenient method for achieving large-area crystals, which is only confined by the amount of materials and the container size. However, the major problem of the melt-recrystallization method is the high growth temperature, which may induce instability of organic semiconductors with oxidation or decomposition. Therefore, the number of reported organic semiconductors suitable for melt-recrystallization is still limited. Among the aforementioned methods, the vapor-processing method is widely adopted for the growth of large-area crystals. However, in order to get large crystal sizes, many complicated growth factors need to be considered, including the source and sublimation temperature, the crystallization area condition, the gas flow, and the temperature gradient, and so forth. Thus, more endeavors for crystal-growth are needed, which are quite pertinent to practical applications and toward boosting the development of OSCS-based devices.

Besides the discovery of laser oscillation and spectrally narrowed emissions in OSCSs, the aim for light amplification upon electrically driven devices is paramount. OLETs utilizing OSCSs as active layers are still the most promising device configuration in this aspect. Notable approaches have been made through controlling the recombination size, operating the device by AC current, and adding modified layers. Even incorporation of different optical resonators to lower the lasing threshold, several more orders of magnitude exciton density are still required to be achieved for realizing lasing behavior. However, the shortage of electrically driven organic lasers will keep on encouraging scientists and inspire them with novel ideas to overcome this challenge.

In summary, we have reviewed recent progress on OSCSs including the intrinsic properties affecting light-emitting behavior, crystal-growth strategies to prepare high-quality OSCSs via solution, melting, and vapor phases, and two major applications, OLEDs and OLETs. The prominent advantages of OSCSs allow the potential for these crystalline materials to go beyond the development of amorphous ones and garner industrial interest. The prerequisites for light-emitting applications are chiefly luminescence properties and charge-transport characteristics where in-depth understanding and thorough investigation are needed. Buoyed by the excellent achievements, it is reasonable to expect that OSCSs will make great progress in future optoelectronic applications.

Acknowledgements

This work was supported by the National Key Research and Development Program of China (Grant No. 2017YFB0404500), the National Natural Science Foundation Program of China (Grant Nos. 61604018, 61675085, 61825402, 61705075, and 61590930), the China Postdoctoral Science Foundation (Grant No. 2015M581377), and the Hong Kong Scholars Program (Grant No. XJ2018004).

Conflict of Interest

The authors declare no conflict of interest.

Keywords

charge-carrier mobility, organic light-emitting diodes, organic light-emitting transistors, organic single-crystalline semiconductors, spectrally narrowed emission

Received: January 7, 2019
Revised: July 3, 2019
Published online: September 10, 2019

[1] A. J. Heeger, *Angew. Chem., Int. Ed.* **2001**, *40*, 2591.
[2] A. J. Heeger, *Chem. Soc. Rev.* **2010**, *39*, 2354.
[3] A. Buckley, *Organic Light-Emitting Diodes (OLEDs): Materials, Devices and Applications*, Elsevier, The Netherlands **2013**.
[4] R. J. Mortimer, A. L. Dyer, J. R. Reynolds, *Displays* **2006**, *27*, 2.
[5] I. D. W. Samuel, G. A. Turnbull, *Chem. Rev.* **2007**, *107*, 1272.
[6] S. Gunes, H. Neugebauer, N. S. Sariciftci, *Chem. Rev.* **2007**, *107*, 1324.
[7] A. C. Grimsdale, K. L. Chan, R. E. Martin, P. G. Jokisz, A. B. Holmes, *Chem. Rev.* **2009**, *109*, 897.
[8] Y. J. Cheng, S. H. Yang, C. S. Hsu, *Chem. Rev.* **2009**, *109*, 5868.
[9] A. C. Arias, J. D. MacKenzie, I. McCulloch, J. Rivnay, A. Salleo, *Chem. Rev.* **2010**, *110*, 3.
[10] P. M. Beaujuge, J. R. Reynolds, *Chem. Rev.* **2010**, *110*, 268.
[11] A. Facchetti, *Chem. Mater.* **2011**, *23*, 733.
[12] C. L. Wang, H. L. Dong, W. P. Hu, Y. Q. Liu, D. B. Zhu, *Chem. Rev.* **2012**, *112*, 2208.
[13] H. Sirringhaus, *Adv. Mater.* **2014**, *26*, 1319.
[14] A. C. Siegel, S. T. Phillips, M. D. Dickey, N. S. Lu, Z. G. Suo, G. M. Whitesides, *Adv. Funct. Mater.* **2010**, *20*, 28.
[15] X. Zhao, S. T. Chaudhry, J. Mei, *Advances in Heterocyclic Chemistry*, Academic Press, Cambridge, MA **2017**.
[16] F. C. Krebs, *Sol. Energy Mater. Sol. Cells* **2009**, *93*, 394.
[17] H. Minemawari, T. Yamada, H. Matsui, J. Tsutsumi, S. Haas, R. Chiba, R. Kumai, T. Hasegawa, *Nature* **2011**, *475*, 364.
[18] R. Sondergaard, M. Hosel, D. Angmo, T. T. Larsen-Olsen, F. C. Krebs, *Mater. Today* **2012**, *15*, 36.
[19] Y. Diao, L. Shaw, Z. A. Bao, S. C. B. Mannsfeld, *Energy Environ. Sci.* **2014**, *7*, 2145.
[20] H. L. Dong, X. L. Fu, J. Liu, Z. R. Wang, W. P. Hu, *Adv. Mater.* **2013**, *25*, 6158.
[21] P. M. Beaujuge, C. M. Amb, J. R. Reynolds, *Acc. Chem. Res.* **2010**, *43*, 1396.
[22] P. M. Beaujuge, J. M. J. Frechet, *J. Am. Chem. Soc.* **2011**, *133*, 20009.
[23] J. Mei, Y. Diao, A. L. Appleton, L. Fang, Z. Bao, *J. Am. Chem. Soc.* **2013**, *135*, 6724.
[24] S. Holliday, J. E. Donaghey, I. McCulloch, *Chem. Mater.* **2014**, *26*, 647.
[25] C. Wang, H. Dong, L. Jiang, W. Hu, *Chem. Soc. Rev.* **2018**, *47*, 422.
[26] S. Hotta, T. Yamao, S. Z. Bisri, T. Takenobu, Y. Iwasa, *J. Mater. Chem. C* **2014**, *2*, 965.
[27] S. Hotta, T. Yamao, *J. Mater. Chem.* **2011**, *21*, 1295.
[28] S. Hotta, *Polym. Int.* **2017**, *66*, 223.
[29] S. Z. Bisri, T. Takenobu, Y. Iwasa, *J. Mater. Chem. C* **2014**, *2*, 2827.
[30] J. Gierschner, S. Varghese, S. Y. Park, *Adv. Opt. Mater.* **2016**, *4*, 348.
[31] A. J. C. Kuehne, M. C. Gather, *Chem. Rev.* **2016**, *116*, 12823.
[32] H. H. Fang, J. Yang, J. Feng, T. Yamao, S. Hotta, H.-B. Sun, *Laser Photonics Rev.* **2014**, *8*, 687.
[33] S. Z. Bisri, C. Piliego, J. Gao, M. A. Loi, *Adv. Mater.* **2014**, *26*, 1176.
[34] H. Dong, X. Fu, J. Liu, Z. Wang, W. Hu, *Adv. Mater.* **2013**, *25*, 6158.
[35] H. Wang, Z. Xie, Y. Ma, J. Shen, *Sci. China, Ser. B: Chem.* **2007**, *50*, 433.
[36] Y. Yuan, G. Giri, A. L. Ayzner, A. P. Zoombelt, S. C. B. Mannsfeld, J. Chen, D. Nordlund, M. F. Toney, J. Huang, Z. Bao, *Nat. Commun.* **2014**, *5*, 3005.
[37] M. Pope, H. P. Kallmann, P. Magnante, *J. Chem. Phys.* **1963**, *38*, 2042.
[38] F. C. Spano, *Annu. Rev. Phys. Chem.* **2006**, *57*, 217.
[39] R. M. Hochstrasser, M. Kasha, *Photochem. Photobiol.* **1964**, *3*, 317.
[40] M. Kasha, *Radiat. Res.* **1963**, *20*, 55.
[41] E. G. McRae, M. Kasha, *J. Chem. Phys.* **1958**, *28*, 721.
[42] F. C. Spano, C. Silva, *Annu. Rev. Phys. Chem.* **2014**, *65*, 477.
[43] F. C. Spano, *J. Chem. Phys.* **2003**, *118*, 981.
[44] S. Siddiqui, F. Spano, *Chem. Phys. Lett.* **1999**, *308*, 99.
[45] F. C. Spano, *Acc. Chem. Res.* **2010**, *43*, 429.
[46] O. Ostroverkhova, *Chem. Rev.* **2016**, *116*, 13279.
[47] J. Cornil, D. A. dos Santos, X. Crispin, R. Silbey, J. L. Brédas, *J. Am. Chem. Soc.* **1998**, *120*, 1289.
[48] J. Cornil, D. Beljonne, J. P. Calbert, J. L. Brédas, *Adv. Mater.* **2001**, *13*, 1053.
[49] R. Marcus, *J. Chem. Phys.* **1956**, *24*, 966.
[50] V. Coropceanu, J. Cornil, D. A. da Silva Filho, Y. Olivier, R. Silbey, J.-L. Brédas, *Chem. Rev.* **2007**, *107*, 926.
[51] L. Wang, G. Nan, X. Yang, Q. Peng, Q. Li, Z. Shuai, *Chem. Soc. Rev.* **2010**, *39*, 423.
[52] J.-L. Brédas, D. Beljonne, V. Coropceanu, *Chem. Rev.* **2004**, *104*, 4971.
[53] R. Kepler, *Phys. Rev.* **1960**, *119*, 1226.
[54] O. H. LeBlanc Jr., *J. Chem. Phys.* **1960**, *33*, 626.
[55] W. Warta, N. Karl, *Phys. Rev. B* **1985**, *32*, 1172.
[56] Y. Guo, G. Yu, Y. Liu, *Adv. Mater.* **2010**, *22*, 4427.
[57] A. Dodabalapur, L. Torsi, H. E. Katz, *Science* **1995**, *268*, 270.
[58] F. Dinelli, M. Murgia, P. Levy, M. Cavallini, F. Biscarini, *Phys. Rev. Lett.* **2004**, *92*, 116802.
[59] M. Kiguchi, M. Nakayama, T. Shimada, K. Saiki, *Phys. Rev. B* **2005**, *71*, 035332.
[60] V. Podzorov, E. Menard, A. Borissov, V. Kiryukhin, J. A. Rogers, M. E. Gershenson, *Phys. Rev. Lett.* **2004**, *93*, 086602.
[61] V. Podzorov, E. Menard, J. A. Rogers, M. E. Gershenson, *Phys. Rev. Lett.* **2005**, *95*, 226601.
[62] E. Menard, V. Podzorov, S.-H. Hur, A. Gaur, M. E. Gershenson, J. A. Rogers, *Adv. Mater.* **2004**, *16*, 2097.
[63] M. Yamagishi, J. Takeya, Y. Tominari, Y. Nakazawa, T. Kuroda, S. Ikehata, M. Uno, T. Nishikawa, T. Kawase, *Appl. Phys. Lett.* **2007**, *90*, 182117.
[64] O. D. Jurchescu, M. Popincuic, B. J. van Wees, T. T. M. Palstra, *Adv. Mater.* **2007**, *19*, 688.
[65] M.-H. Yoon, S. A. DiBenedetto, A. Facchetti, T. J. Marks, *J. Am. Chem. Soc.* **2005**, *127*, 1348.
[66] Y. Sakamoto, T. Suzuki, M. Kobayashi, Y. Gao, Y. Fukai, Y. Inoue, F. Sato, S. Tokito, *J. Am. Chem. Soc.* **2004**, *126*, 8138.
[67] G. Nan, L. Wang, X. Yang, Z. Shuai, Y. Zhao, *J. Chem. Phys.* **2009**, *130*, 024704.
[68] H. Nakanotani, M. Saito, H. Nakamura, C. Adachi, *Appl. Phys. Lett.* **2009**, *95*, 103307.
[69] D. Fichou, S. Delysse, J. M. Nunzi, *Adv. Mater.* **1997**, *9*, 1178.
[70] D. Fichou, B. Bachet, F. Demanze, I. Billy, G. Horowitz, F. Garnier, *Adv. Mater.* **1996**, *8*, 500.
[71] D. Fichou, F. Demanze, G. Horowitz, R. Hajlaoui, M. Constant, F. Gamier, *Synth. Met.* **1997**, *85*, 1309.
[72] G. Horowitz, F. Kouki, A. E. Kassmi, P. Valat, V. Wintgens, F. Garnier, *Adv. Mater.* **1999**, *11*, 234.
[73] D. Fichou, M. P. te Ulade-Fichou, G. Horowitz, F. Demanze, *Adv. Mater.* **1997**, *9*, 75.
[74] G. Horowitz, S. Romdhane, H. Bouchriha, P. Delannoy, J.-L. Monge, F. Kouki, P. Valat, *Synth. Met.* **1997**, *90*, 187.
[75] D. Fichou, *J. Mater. Chem.* **2000**, *10*, 571.
[76] H. Yanagi, T. Morikawa, *Appl. Phys. Lett.* **1999**, *75*, 187.
[77] H. Yanagi, T. Ohara, T. Morikawa, *Adv. Mater.* **2001**, *13*, 1452.
[78] A. Andreev, G. Matt, C. J. Brabec, H. Sitter, D. Badt, H. Seyringer, N. S. Sariciftci, *Adv. Mater.* **2000**, *12*, 629.
[79] A. Andreev, F. Quochi, A. Kadashchuk, H. Sitter, C. Winder, H. Hoppe, S. Sariciftci, A. Mura, G. Bongiovanni, *Phys. Status Solidi A* **2004**, *201*, 2288.
[80] F. Quochi, A. Andreev, F. Cordella, R. Orru, A. Mura, G. Bongiovanni, H. Hoppe, H. Sitter, N. S. Sariciftci, *J. Lumin.* **2005**, *112*, 321.
[81] A. Kadashchuk, A. Andreev, H. Sitter, N. S. Sariciftci, Y. Skryshevski, Y. Piryatinski, I. Blonsky, D. Meissner, *Adv. Funct. Mater.* **2004**, *14*, 970.

[82] F. Hide, B. J. Schwartz, M. A. Díaz-García, A. J. Heeger, *Chem. Phys. Lett.* **1996**, *256*, 424.
[83] C. C. Wu, O. J. Korovyanko, M. C. Delong, Z. V. Vardeny, J. P. Ferraris, *Synth. Met.* **2003**, *139*, 735.
[84] R. Kabe, H. Nakanotani, T. Sakanoue, M. Yahiro, C. Adachi, *Adv. Mater.* **2009**, *21*, 4034.
[85] Y. P. Li, F. Li, H. Y. Zhang, Z. Q. Xie, W. J. Xie, H. Xu, B. Li, F. Z. Shen, L. Ye, M. Hanif, D. G. Ma, Y. G. Ma, *Chem. Commun.* **2007**, *3*, 231.
[86] Y. P. Li, F. Z. Shen, H. Wang, F. He, Z. Q. Xie, H. Y. Zhang, Z. M. Wang, L. L. Liu, F. Li, M. Hanif, L. Ye, Y. G. Ma, *Chem. Mater.* **2008**, *20*, 7312.
[87] Z. Q. Xie, L. L. Liu, B. Yang, G. D. Yang, L. Ye, M. Li, Y. G. Ma, *Cryst. Growth Des.* **2005**, *5*, 1959.
[88] Z. Q. Xie, H. Wang, F. Li, W. J. Xie, L. L. Liu, B. Yang, L. Ye, Y. G. Ma, *Cryst. Growth Des.* **2007**, *7*, 2512.
[89] H. Wang, Z. Q. Xie, B. Yang, F. Z. Shen, Y. P. Li, Y. G. Ma, *CrystEngComm* **2008**, *10*, 1252.
[90] H. Wang, F. Li, I. Ravia, B. Gao, Y. Li, V. Medvedev, H. Sun, N. Tessler, Y. Ma, *Adv. Funct. Mater.* **2011**, *21*, 3770.
[91] Z. Q. Xie, W. J. Xie, F. Li, L. L. Liu, H. Wang, Y. G. Ma, *J. Phys. Chem. C* **2008**, *112*, 9066.
[92] Z. Q. Xie, B. Yang, L. L. Liu, M. Li, D. Lin, Y. G. Ma, G. Cheng, S. Y. Liu, *J. Phys. Org. Chem.* **2005**, *18*, 962.
[93] S. Hotta, S. Lee, T. Tamaki, *J. Heterocycl. Chem.* **2000**, *37*, 25.
[94] S. Hotta, *J. Heterocycl. Chem.* **2001**, *38*, 923.
[95] S. Hotta, T. Katagiri, *J. Heterocycl. Chem.* **2003**, *40*, 845.
[96] T. Katagiri, S. Ota, T. Ohira, T. Yamao, S. Hotta, *J. Heterocycl. Chem.* **2007**, *44*, 853.
[97] T. Dingemans, A. Bacher, M. Thelakkat, L. Pedersen, E. Samulski, H.-W. Schmidt, *Synth. Met.* **1999**, *105*, 171.
[98] R. Hibino, M. Nagawa, S. Hotta, M. Ichikawa, T. Koyama, Y. Taniguchi, *Adv. Mater.* **2002**, *14*, 119.
[99] M. Ichikawa, K. Nakamura, M. Inoue, H. Mishima, T. Haritani, R. Hibino, T. Koyama, Y. Taniguchi, *Appl. Phys. Lett.* **2005**, *87*, 221113.
[100] Y. Yomogida, T. Takenobu, H. Shimotani, K. Sawabe, S. Z. Bisri, T. Yamao, S. Hotta, Y. Iwasa, *Appl. Phys. Lett.* **2010**, *97*, 173301.
[101] H. Mizuno, I. Ohnishi, H. Yanagi, F. Sasaki, S. Hotta, *Adv. Mater.* **2012**, *24*, 2404.
[102] S. Z. Bisri, T. Takenobu, Y. Yomogida, H. Shimotani, T. Yamao, S. Hotta, Y. Iwasa, *Adv. Funct. Mater.* **2009**, *19*, 1728.
[103] S. Kanazawa, M. Ichikawa, T. Koyama, Y. Taniguchi, *ChemPhysChem* **2006**, *7*, 1881.
[104] M. Nagawa, R. Hibino, S. Hotta, H. Yanagi, M. Ichikawa, T. Koyama, Y. Taniguchi, *Appl. Phys. Lett.* **2002**, *80*, 544.
[105] M. Ichikawa, R. Hibino, M. Inoue, T. Haritani, S. Hotta, T. Koyama, Y. Taniguchi, *Adv. Mater.* **2003**, *15*, 213.
[106] S. Hotta, H. Kimura, S. A. Lee, T. Tamaki, *J. Heterocycl. Chem.* **2000**, *37*, 281.
[107] K. Shimizu, D. Hoshino, S. Hotta, *Appl. Phys. Lett.* **2003**, *83*, 4494.
[108] S. Kobayashi, F. Sasaki, H. Yanagi, S. Hotta, M. Ichikawa, Y. Taniguchi, *J. Lumin.* **2005**, *112*, 325.
[109] K. Bando, T. Nakamura, S. Fujiwara, Y. Masumoto, F. Sasaki, S. Kobayashi, Y. Shimoi, S. Hotta, *Phys. Rev. B* **2008**, *77*, 045205.
[110] H. Mizuno, U. Haku, Y. Marutani, A. Ishizumi, H. Yanagi, F. Sasaki, S. Hotta, *Adv. Mater.* **2012**, *24*, 5744.
[111] H. Yanagi, A. Yoshiki, S. Hotta, S. Kobayashi, *J. Appl. Phys.* **2004**, *96*, 4240.
[112] Y. Wang, R. Kumashiro, Z. Li, R. Nouchi, K. Tanigki, *Appl. Phys. Lett.* **2009**, *95*, 103306.
[113] S. Hotta, T. Yamao, T. Katagiri, *J. Nanosci. Nanotechnol.* **2014**, *14*, 2102.
[114] J. Luo, Z. Xie, J. W. Y. Lam, L. Cheng, H. Chen, C. Qiu, H. S. Kwok, X. Zhan, Y. Liu, D. Zhu, B. Z. Tang. *Chem. Commun.* **2001**, *18*, 1740.
[115] B. K. An, S. K. Kwon, S. D. Jung, S. Y. Park. *J. Am. Chem. Soc.* **2002**, *124*, 14410.
[116] J. Chen, C. C. W. Law, J. W. Y. Lam, Y. Dong, S. M. F. Lo, *Chem. Mater.* **2003**, *15*, 1535.
[117] H. Wang, F. Li, B. Gao, Z. Xie, S. Liu, C. Wang, D. Hu, F. Shen, Y. Xu, H. Shang, Q. Chen, Y. Ma, H. B. Sun, *Cryst. Growth Des.* **2009**, *9*, 4945.
[118] H. Nakanotani, M. Saito, H. Nakamura, C. Adachi, *Adv. Funct. Mater.* **2010**, *20*, 1610.
[119] H. Nakanotani, C. Adachi, *Adv. Opt. Mater.* **2013**, *1*, 422.
[120] H. H. Fang, S. Y. Lu, L. Wang, R. Ding, H. Y. Wang, J. Feng, Q. D. Chen, H. B. Sun, *Org. Electron.* **2013**, *14*, 389.
[121] H. Wang, B. Yue, Z. Xie, B. Gao, Y. Xu, L. Liu, H. B. Sun, Y. Ma, *Phys. Chem. Chem. Phys.* **2013**, *15*, 3527.
[122] M. Ichikawa, R. Hibino, M. Inoue, T. Haritani, S. Hotta, K. Araki, T. Koyama, Y. Taniguchi, *Adv. Mater.* **2005**, *17*, 2073.
[123] S. Hotta, Y. Sakurai, Y. Okuda, T. Miki, K. Matsunaga, F. Hirato, T. Yanao, H. Jinnai, *J. Nanosci. Nanotechnol.* **2010**, *10*, 440.
[124] K. Shimizu, Y. Mori, S. Hotta, *J. Appl. Phys.* **2006**, *99*, 063505.
[125] T. Yamao, K. Yamamoto, Y. Taniguchi, T. Miki, S. Hotta, *J. Appl. Phys.* **2008**, *103*, 093115.
[126] T. Yamao, K. Yamamoto, T. Inoue, Y. Okuda, Y. Taniguchi, S. Hotta, *Jpn. J. Appl. Phys.* **2009**, *48*, 04C174.
[127] T. Yamao, K. Yamamoto, S. Hotta, *J. Nanosci. Nanotechnol.* **2009**, *9*, 2582.
[128] H. Mizuno, T. Maeda, H. Yanagi, H. Katsuki, M. Aresti, F. Quochi, M. Saba, A. Mura, G. Bongiovanni, F. Sasaki, S. Hotta, *Adv. Opt. Mater.* **2014**, *2*, 529.
[129] F. Quochi, F. Cordella, A. Mura, G. Bongiovanni, F. Balzer, H. G. Rubahn, *J. Phys. Chem. B* **2005**, *109*, 21690.
[130] Y. S. Zhao, A. D. Peng, H. B. Fu, Y. Ma, J. N. Yao, *Adv. Mater.* **2008**, *20*, 1661.
[131] S. M. Yoon, J. Lee, J. H. Je, H. C. Choi, M. Yoon, *ACS Nano* **2011**, *5*, 2923.
[132] H. H. Fang, R. Ding, S. Y. Lu, J. Yang, X. L. Zhang, R. Yang, J. Feng, Q. D. Chen, J. F. Song, H. B. Sun, *Adv. Funct. Mater.* **2012**, *22*, 33.
[133] R. Ding, H. H. Fang, Y. Wang, S. Y. Lu, X. L. Zhang, L. Wang, J. Feng, Q. D. Chen, H. B. Sun, *Org. Electron.* **2012**, *13*, 1602.
[134] H. H. Fang, R. Ding, S. Y. Lu, X. L. Zhang, J. Feng, H. B. Sun, *J. Mater. Chem.* **2012**, *22*, 24139.
[135] H. Yamamoto, K. Obara, S. Higashihara, Y. Obama, T. Yamao, S. Hotta, *J. Nanosci. Nanotechnol.* **2016**, *16*, 3312.
[136] H. H. Fang, R. Ding, S. Y. Lu, Y. D. Yang, Q. D. Chen, J. Feng, Y. Z. Huang, H. B. Sun, *Laser Photonics Rev.* **2013**, *7*, 281.
[137] V. C. Sundar, J. Zaumseil, V. Podzorov, E. Menard, R. L. Willett, T. Someya, M. E. Gershenson, J. A. Rogers, *Science* **2004**, *303*, 1644.
[138] H. Jiang, K. K. Zhang, J. Ye, F. Wei, P. Hu, J. Guo, C. Liang, X. Chen, Y. Zhao, L. E. McNeil, W. Hu, C. Kloc, *Small* **2013**, *9*, 990.
[139] L. Jiang, W. Hu, Z. Wei, W. Xu, H. Meng, *Adv. Mater.* **2009**, *21*, 3649.
[140] T. He, X. Zhang, J. Jia, Y. Li, X. Tao, *Adv. Mater.* **2012**, *24*, 2171.
[141] H. H. Fang, Q. D. Chen, J. Yang, H. Xia, Y. G. Ma, H. Y. Wang, H. B. Sun, *Opt. Lett.* **2010**, *35*, 441.
[142] T. Yamao, T. Ohira, S. Ota, S. Hotta, *J. Appl. Phys.* **2007**, *101*, 083517.
[143] A. Rizzo, C. Nobile, M. Mazzeo, M. D. Giorgi, A. Fiore, L. Carbone, R. Cingolani, L. Manna, G. Gigli, *ACS Nano* **2009**, *3*, 1506.
[144] T. Yamao, Y. Taniguchi, K. Yamamoto, T. Miki, T. Ohira, S. Hotta, *Jpn. J. Appl. Phys.* **2008**, *47*, 4719.
[145] T. Yamao, Y. Okuda, Y. Makino, S. Hotta, *J. Appl. Phys.* **2011**, *110*, 053113.

[146] T. Yamao, Y. Taniguchi, K. Yamamoto, T. Miki, S. Ota, S. Hotta, M. Goto, R. Azumi, *Jpn. J. Appl. Phys.* **2007**, *46*, 7478.
[147] H. Jiang, C. Kloc, *MRS Bull.* **2013**, *38*, 28.
[148] D. H. Kim, D. Y. Lee, H. S. Lee, W. H. Lee, Y. H. Kim, J. I. Han, K. Cho, *Adv. Mater.* **2007**, *19*, 678.
[149] K. Balakrishnan, A. Datar, R. Oitker, H. Chen, J. Zuo, L. Zang, *J. Am. Chem. Soc.* **2005**, *127*, 10496.
[150] M. Mas-Torrent, P. Hadley, S. T. Bromley, X. Ribas, J. Tarrés, M. Mas, E. Molins, J. Veciana, C. Rovira, *J. Am. Chem. Soc.* **2004**, *126*, 8546.
[151] M. Mas-Torrent, P. Hadley, S. T. Bromley, N. Crivillers, J. Veciana, C. Rovira, *Appl. Phys. Lett.* **2005**, *86*, 012110.
[152] X. Mu, W. Song, Y. Zhang, K. Ye, H. Zhang, Y. Wang, *Adv. Mater.* **2010**, *22*, 4905.
[153] C. Liu, Y. Li, Y. Xu, T. Minari, S. Li, K. Takimiya, K. Tsukagoshi, *Org. Electron.* **2012**, *13*, 2975.
[154] J. Jang, S. Nam, K. Im, J. Hur, S. N. Cha, J. Kim, H. B. Son, H. Suh, M. A. Loth, J. E. Anthony, J.-J. Park, C. E. Park, J. M. Kim, K. Kim, *Adv. Funct. Mater.* **2012**, *22*, 1005.
[155] X. Zhang, J. Jie, W. Deng, Q. Shang, J. Wang, H. Wang, X. Chen, X. Zhang, *Adv. Mater.* **2016**, *28*, 2475.
[156] M. Cavallini, P. D'Angelo, V. V. Criado, D. Gentili, A. Shehu, F. Leonardi, S. Milita, F. Liscio, F. Biscarini, *Adv. Mater.* **2011**, *23*, 5091.
[157] M. Cavallini, P. Stoliar, J.-F. Moulin, M. Surin, P. Leclere, R. Lazzaroni, D. W. Breiby, J. W. Andreasen, M. M. Nielsen, P. Sonar, A. C. Grimsdale, K. Mullen, F. Biscarini, *Nano Lett.* **2005**, *5*, 2422.
[158] R.-R. Bao, C.-Y. Zhang, X. J. Zhang, X.-M. Ou, C.-S. Lee, J.-S. Jie, X.-H. Zhang, *ACS Appl. Mater. Interfaces* **2013**, *5*, 5757.
[159] T. Yamao, T. Miki, H. Akagami, Y. Nishimoto, S. Ota, S. Hotta, *Chem. Mater.* **2007**, *19*, 3748.
[160] Y. Inada, T. Yamao, M. Inada, T. Itami, S. Hotta, *Synth. Met.* **2011**, *161*, 1869.
[161] H. Figi, M. Jazbinsek, C. Hunziker, M. Koechlin, P. Gunter, *Opt. Express* **2008**, *16*, 11310.
[162] H. Figi, M. Jazbinsek, C. Hunziker, M. Koechlin, P. Gunter, *J. Opt. Soc. Am. B* **2009**, *26*, 1103.
[163] O. P. Kwon, B. Ruiz, A. Choubey, L. Mutter, A. Schneider, M. Jazbinsek, V. Gramlich, P. Gunter, *Chem. Mater.* **2006**, *18*, 4049.
[164] S. Tavazzi, L. Miozzo, L. Silvestri, S. Mora, P. Spearman, M. Moret, S. Rizzato, D. Braga, A. K. D. Diaw, D. Gningue-Sall, J. J. Aaron, A. Yassar, *Cryst. Growth Des.* **2010**, *10*, 2342.
[165] F. Sasaki, M. Mori, S. Haraichi, Y. Ido, Y. Masumoto, S. Hotta, *Org. Electron.* **2010**, *11*, 1192.
[166] F. Sasaki, S. Kobayashi, S. Haraichi, S. Fujiwara, K. Bando, Y. Masumoto, S. Hotta, *Adv. Mater.* **2007**, *19*, 3653.
[167] J. Ribierre, Z. Li, X. Liu, E. Lacaze, B. Heinrich, S. Méry, P. Sleczkowski, Y. Xiao, F. Lafolet, D. Hashizume, T. Aoyama, M. Uchiyama, J. W. Wu, E. Zaborova, F. Fages, A. D'Aléo, F. Mathevet, C. Adachi, *J. Mater. Chem. C* **2019**, *7*, 3190.
[168] H. Bi, H. Zhang, Y. Zhang, H. Gao, Z. Su, Y. Wang, *Adv. Mater.* **2010**, *22*, 1631.
[169] H. Zhang, Z. Zhang, K. Ye, J. Zhang, Y. Wang, *Adv. Mater.* **2006**, *18*, 2369.
[170] Y. Zhao, H. Gao, Y. Fan, T. Zhou, Z. Su, Y. Liu, Y. Wang, *Adv. Mater.* **2009**, *21*, 6165.
[171] A. Inoue, T. Okamoto, M. Sakai, S. Kuniyoshi, H. Yamauchi, M. Nakamura, K. Kudo, *Phys. Status Solidi A* **2013**, *210*, 1353.
[172] H. M. Lee, J. J. Kim, J. H. Choi, S. O. Cho, *ACS Nano* **2011**, *5*, 8352.
[173] N. Karl, *J. Cryst. Growth* **1990**, *99*, 1009.
[174] R. A. Laudise, C. Kloc, P. G. Simpkins, T. Siegrist, *J. Cryst. Growth* **1998**, *187*, 449.
[175] T. Yamao, K. Juri, A. Kamoi, S. Hotta, *Org. Electron.* **2009**, *10*, 1241.
[176] J. Yang, H. H. Fang, R. Ding, S. Y. Lu, Y. L. Zhang, Q. D. Chen, H. B. Sun, *J. Phys. Chem. C* **2011**, *115*, 9171.
[177] L. Briseno, S. C. B. Mannsfeld, M. M. Ling, S. H. Liu, R. J. Tseng, C. Reese, M. E. Roberts, Y. Yang, F. Wudl, Z. N. Bao, *Nature* **2006**, *444*, 913.
[178] F. J. M. Zu Heringdorf, M. C. Reuter, R. M. Tromp, *Nature* **2001**, *412*, 517.
[179] R. Ruiz, D. Choudhary, B. Nichel, T. Toccoli, K.-C. Chang, A. C. Mayer, P. Clancy, J. M. Blakely, R. L. Headrick, S. Iannotta, G. G. Malliaras, *Chem. Mater.* **2004**, *16*, 4497.
[180] J. W. Lee, K. Kim, D. H. Park, M. Y. Cho, Y. B. Lee, J. S. Jung, D.-C. Kim, J. Kim, J. Joo, *Adv. Funct. Mater.* **2009**, *19*, 704.
[181] Y. Takeyama, S. Maruyama, Y. Matsumoto, *Cryst. Growth Des.* **2011**, *11*, 2273.
[182] Y. Takeyama, S. Ono, Y. Matsumoto, *Appl. Phys. Lett.* **2012**, *101*, 083303.
[183] Y. S. Xhao, C. Di, W. Yang, G. Yu, Y. Liu, J. Yao, *Adv. Funct. Mater.* **2006**, *16*, 1985.
[184] M. Yilmaz, M. Ozdemir, H. Erdogan, U. Tamer, U. Sen, A. Facchetti, H. Usta, G. Demirel, *Adv. Funct. Mater.* **2015**, *25*, 5669.
[185] H. Yanagi, T. Morikawa, *Appl. Phys. Lett.* **2002**, *81*, 1512.
[186] K. W. Yee, M. Yokoyama, M. Hiramoto, *Appl. Phys. Lett.* **2006**, *88*, 083511.
[187] X. Li, Y. Xu, F. Li, Y. Ma, *Org. Electron.* **2012**, *13*, 762.
[188] H. Nakanotani, C. Adachi, *Appl. Phys. Lett.* **2010**, *96*, 053301.
[189] R. Ding, J. Feng, X. L. Zhang, W. Zhou, H. H. Fang, Y. F. Liu, Q. D. Chen, H. Y. Wang, H. B. Sun, *Adv. Funct. Mater.* **2014**, *24*, 7085.
[190] R. Ding, J. Feng, W. Zhou, X. L. Zhang, H. H. Fang, T. Yang, H. Y. Wang, S. Hotta, H. B. Sun, *Sci. Rep.* **2015**, *5*, 12445.
[191] F.-X. Dong, R. Ding, S. Hotta, A.-W. Li, *Opt. Commun.* **2017**, *392*, 247.
[192] R. Ding, J. Feng, F. X. Dong, W. Zhou, Y. Liu, X. L. Zhang, X. P. Wang, H. H. Fang, B. Xu, X. B. Li, H. Y. Wang, S. Hotta, H. B. Sun, *Adv. Funct. Mater.* **2017**, *27*, 1604659.
[193] R. Ding, X. P. Wang, J. Feng, X. B. Li, F. X. Dong, W. Q. Tian, J. R. Du, H. H. Fang, H. Y. Wang, T. Yamao, S. Hotta, H. B. Sun, *Adv. Mater.* **2018**, *30*, 1801078.
[194] R. Ding, F. X. Dong, M. H. An, X. P. Wang, M. R. Wang, X. B. Li, J. Feng, H. B. Sun, *Adv. Funct. Mater.* **2019**, *29*, 1807606.
[195] A. Hepp, H. Heil, W. Weise, M. Ahles, R. Schmechel, H. von Seggern, *Phys. Rev. Lett.* **2003**, *91*, 157406.
[196] K. Nakamura, M. Ichikawa, R. Fushiki, T. Kamikawa, M. Inoue, T. Koyama, Y. Taniguchi, *Jpn. J. Appl. Phys.* **2005**, *44*, L1367.
[197] T. Yamao, Y. Shimizu, K. Terasaki, S. Hotta, *Adv. Mater.* **2008**, *20*, 4109.
[198] T. Katagiri, Y. Shimizu, K. Terasaki, T. Yamao, S. Hotta, *Org. Electron.* **2011**, *12*, 8.
[199] T. Yamao, K. Terasaki, Y. Shimizu, S. Hotta, *J. Nanosci. Nanotechnol.* **2010**, *10*, 1017.
[200] T. Takahashi, T. Takenobu, J. Takeya, Y. Iwasa, *Adv. Funct. Mater.* **2007**, *17*, 1623.
[201] K. Sawabe, T. Takenobu, S. Z. Bisri, T. Yamao, S. Hotta, Y. Iwasa, *Appl. Phys. Lett.* **2010**, *97*, 043307.
[202] T. Takenobu, S. Z. Bisri, T. Takahashi, M. Yahiro, C. Adachi, Y. Iwasa, *Phys. Rev. Lett.* **2008**, *100*, 066601.
[203] H. Nakanotani, R. Kabe, M. Yahiro, T. Takenobu, Y. Iwasa, C. Adachi, *Appl. Phys. Express* **2008**, *1*, 091801.
[204] S. Z. Bisri, T. Takenobu, K. Sawabe, S. Tsuda, Y. Yomogidao, T. Yamao, S. Hotta, C. Adachi, Y. Iwasa, *Adv. Mater.* **2011**, *23*, 2753.
[205] K. Kajiwara, K. Terasaki, T. Yamao, S. Hotta, *Adv. Funct. Mater.* **2011**, *21*, 2854.

[206] H. Nakanotani, H. Kakizoe, C. Adachi, *Solid State Commun.* **2011**, *151*, 93.
[207] K. Sawabe, M. Imakawa, M. Nakano, T. Yamao, S. Hotta, Y. Iwasa, T. Takenobu, *Adv. Mater.* **2012**, *24*, 6141.
[208] K. Yamada, T. Yamao, S. Hotta, *Adv. Mater.* **2013**, *25*, 2860.
[209] A. Okada, Y. Makino, S. Hotta, T. Yamao, *Phys. Status Solidi C* **2012**, *9*, 2545.
[210] T. Yamao, Y. Sakurai, K. Terasaki, Y. Shimizu, H. Jinnai, S. Hotta, *Adv. Mater.* **2010**, *22*, 3708.
[211] K. Maruyama, K. Sawabe, T. Sakanoue, J. Li, W. Takahashi, S. Hotta, Y. Iwasa, T. Takenobu, *Sci. Rep.* **2015**, *5*, 10221.
[212] S. Z. Bisri, K. Sawabe, M. Imakawa, K. Maruyama, T. Yamao, S. Hotta, Y. Iwasa, T. Takenobu, *Sci. Rep.* **2012**, *2*, 985.
[213] X. Zhang, H. Dong, W. Hu, *Adv. Mater.* **2018**, *30*, 1801048.